ChemComm

Excited-State Structural Dynamics of Nickel Complexes Probed by Optical and X-ray Transient Spectroscopies: Insights and Implications

Journal:	*ChemComm*
Manuscript ID	CC-FEA-07-2021-003875.R1
Article Type:	Feature Article

ARTICLE

Excited-State Structural Dynamics of Nickel Complexes Probed by Optical and X-ray Transient Absorption Spectroscopies: Insights and Implications

Received 00th January 20xx,
Accepted 00th January 20xx

DOI: 10.1039/x0xx00000x

Brian T. Phelan,[a] Michael W. Mara[b] and Lin X. Chen*[a,b]

Excited states of nickel complexes undergo a variety of photochemical processes, such as charge transfer, ligation/deligation, and redox reactions, relevant to solar energy conversion and photocatalysis. The efficiencies of the aforementioned processes are closely coupled to the molecular structures in the ground and excited states. The conventional optical transient absorption spectroscopy has revealed important excited-state pathways and kinetics, but information regarding the metal center, in particular transient structural and electronic properties, remains limited. These deficiencies are addressed by X-ray transient absorption (XTA) spectroscopy, a detailed probe of 3d orbital occupancy, oxidation state and coordination geometry. The examples of excited-state structural dynamics of nickel porphyrin and nickel phthalocyanine have been described from our previous studies with highlights on the unique structural information obtained by XTA spectroscopy. We close by surveying perspective applications of XTA spectroscopy to active areas of Ni-based photocatalysis based on the knowledge gained from our previous studies.

Outline

1. Introduction

Transition metal complexes, due to their versatile properties in photochemical reactions (Figure 1), have been extensively studied as light sensitizers for solar energy conversion, redox centers for photo/electrochemical catalysis, and emitters for optoelectronic devices.[1-11] The direct involvement of the *d* electrons in photophysical and photochemical processes of excited transition metal complexes enables various possibilities of tailoring the metal centers, ligands and stereo effects for the aforementioned applications. Meanwhile, electronic transitions in transition metal complexes often have an intricate mix of metal, ligand, metal-ligand, ligand-ligand and metal-metal character. Moreover, interplays between the energetics and kinetics on the excited-state potential energy surfaces ultimately determine reaction pathways and outcomes. Therefore, correlations between excited-state energetics, kinetics and structures along the reaction trajectories must be disentangled.

The energetics of the excited states could be obtained by conventional UV-vis spectroscopy combined with quantum mechanical calculations to properly assign each transition relevant to photochemical processes. However, this appears to be a challenging endeavor due to the convoluted nature of transition metal complex absorbance spectra and the small oscillator strengths for transitions involving spin state changes or within the *d* or *f* orbital manifolds. Given the variety of excited-state processes observed in transition metal complexes spanning ten or more orders of magnitude in time (Figure 1), the excited-state kinetics are commonly interrogated by time-resolved optical and vibrational spectroscopies, including femtosecond pump-probe optical transient absorption (OTA) spectroscopy,[12-21] femtosecond transient infrared spectroscopy, femtosecond stimulated Raman spectroscopy,[22, 23], and more recently, multiple dimensional spectroscopy, such as two-dimensional electronic and infrared spectroscopy[24-28] and two-dimensional electronic-vibrational spectroscopy.[29, 30] Excited-state structural information of transition metal complexes can be inferred from vibrational spectra, but most of the observed features correspond to the ligand modes and the direct electronic configuration or coordination geometry of the

[a] Chemical Sciences and Engineering Division, Argonne National Laboratory, Lemont, Illinois 60439, United States of America.
[b] Department of Chemistry, Northwestern University, Evanston, Illinois 60208, United States of America.
* Corresponding author, Email: lchen@anl.gov

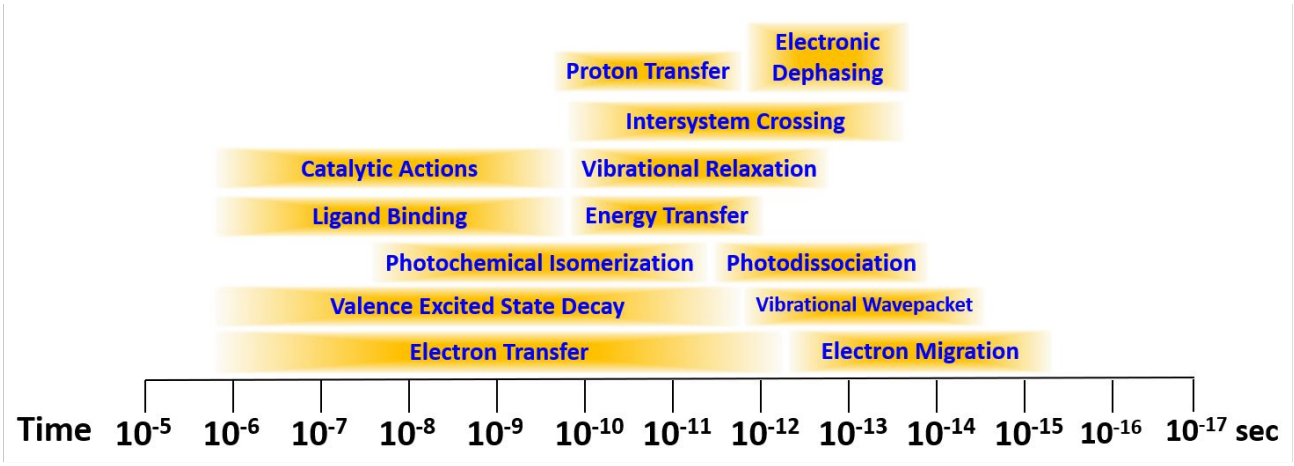

Figure 1. Summary of time scales in photochemical and photophysical processes of transition metal complexes.

metal center is challenging to obtain. Thus, methods that simultaneously obtain functional electronic and coordination structures of the metal centers in transition metal complex excited states are important to facilitate the guided design of optimal photocatalytic systems.

Since the turn of the century, intense pulsed X-ray sources have emerged around the world from third-generation synchrotrons and X-ray free electron lasers, providing X-ray pulses with durations of tens of picoseconds and tens of femtoseconds, respectively. Such X-ray sources have brought a new phase in studying excited-state transition metal complexes and their related applications. Analogous to OTA, or "pump-probe", spectroscopy, a laser pulse initiates a photochemical or photophysical process and an X-ray probe pulse interrogates the response of the system as a function of the delay time between the pump and probe pulses.[16, 31-40] One aspect of this optical-laser pump/X-ray probe approach is the versatility of X-ray photons that induce transitions from the inner shell electrons, such as 1s, 2s, 2p, 3s, 3p, 3d, to higher energy orbitals and the continuum.[41] Similar to the valence transitions probed in the UV-vis, these inner shell transitions also result in emissions when the electrons in the outer shells refill the core holes in the inner shells. These electronic transitions differ from the valence electronic transitions probed by optical absorption and emission spectroscopies, because they are element-specific, atomically localized transitions. Therefore, X-ray absorption and emission spectroscopies are particularly suitable for probing the electronic structures of metal centers, including the electronic occupation, spin state and oxidation state, which often have weak optical signatures in the UV-vis region and are often overwhelmed by the π-π* transition features with much higher oscillator strengths. In addition, X-ray absorption/emission spectroscopy is not restricted to specific sample forms, enabling measurements from gas to solid (amorphous, powder) phases.

Another important feature of X-ray photons is their atomic-scale wavelengths, which enabled the broad use for direct measurements of nuclear structures around the X-ray absorbing atoms with atomic resolution, even imaging the electron densities of atomic orbitals using high energy X-ray diffraction. The remarkable discovery of coherent interference of outgoing and backscattering photoelectron waves laid the foundation for extended X-ray absorption fine structure (EXAFS),[41] which provides high spatial resolution of the local bonding interactions of the interrogated metal centers and, thus, a powerful way to track excited-state structural evolution. In this perspective, we focus on applications of X-ray transient absorption (XTA) spectroscopy, including X-ray absorption near edge structure (XANES) and EXAFS, on excited and transient structures of Ni-based transition metal complexes. The former reveals the electronic structures around the metal centers, and the latter the nuclear structures. Using nickel porphyrin and nickel phthalocyanine as examples, we will demonstrate the current capabilities of studying transition-metal-complex excited-state electronic and nuclear structural dynamics using XTA spectroscopy[34-36, 40, 42] combined with OTA measurements to analyze photochemical and photophysical processes. The knowledge learned from these studies can be utilized in studying transient structures in a broad range of transition metal complexes that are active in photo- and electrocatalysis and could guide synthetic work in optimizing photochemical processes.

In order to demonstrate the capabilities of X-ray transient absorption in studying excited-state transition metal complexes, we choose metalloporphyrins and metallophthalocyanines as examples because their rich photophysical and photochemical pathways are representative of those occurring in transition metal complexes. Moreover, metalloporphyrins are analogs of chromophores in both natural photosynthesis[43-47] and hemeproteins[48-51] and metalloporphyrins and metallophthalocyanines have found many ongoing and potential applications in solar energy conversion, photocatalysis, and optoelectronics. Thus, these molecules have been the focus of countless studies over the past several decades, which accumulated substantial knowledge regarding the electronic and nuclear structure and dynamics of these complexes.[52] Many of these photochemical processes involve excited states of metalloporphyrins and

metallophthalocyanines that are capable of using excess energy and charge to promote chemical reactions.[53-57] In photocatalytic and electrocatalytic reactions, one aims to control the excited-state electron-transfer pathway and rates to favor the productive redox reactions. This, however, is challenging since the dynamics involving the spin state, electronic occupation of the *d* orbitals and coordination geometry are sometimes intertwined, even on the femtosecond timescale following photoexcitation.

The ligation states of these metalloporphyrins and metallophthalocyanines, key intermediates in transition metal complex catalysis, are also diverse and result from the energetics of the molecular orbitals, which are strongly coupled with the coordination geometry and the spin state of the metal center.[58-61] Photocatalysis performed by these molecules often involves axial ligation of substrates at the metal center, where redox reactions and bond forming or breaking can occur.[62, 63] Axial ligation dynamics are strongly dependent on the electronic configurations of metal centers and stereo hindrance of the macrocycles, which can thus be used to regulate photocatalytic processes given sufficient knowledge of the excited-state processes. Thus, it is desirable to understand the correlation of the electronic and nuclear structures of the transient states in metalloporphyrins and metallophthalocyanines with the rates of ligation and redox reactions. The examples included here demonstrate how XTA studies can enhance our understanding of excited-state processes in these molecules, as well as potential applications in molecular design of other transition metal complexes for effective photocatalytic reactions.

In this perspective, we will review the work on structural dynamics of excited-state nickel porphyrin and phthalocyanine without and with the solvent ligation. The interplays of the electronic transition and resultant nuclear structural changes will be described. In particular, we will emphasize the structural information captured by the XTA method and the importance of complementary studies of OTA and XTA for these example transition metal complexes. The comparative studies of these two types of molecules provide important information on the structural influence of the macrocycle environments on photochemistry that have not been observed before. Finally, recent studies on nickel-centered photocatalysts will be presented in connection with the XTA studies to project the impacts of such studies in deciphering structural dynamics of photocatalysts.

2. Electronic Configurations and Nuclear Structures of Excited-State Nickel Porphyrin

Open-shell transition metal porphyrins, such as Ni(II) porphyrins, were not initially considered as building blocks for solar energy conversion because of their fast excited-state deactivation through *d*-orbital vacancies.[64-70] However, they provide a versatile platform to investigate and rationally control these ultrafast deactivation mechanisms given the strong porphyrin-based π → π* transitions, which can funnel energy and/or redox equivalents to the metal centers via internal conversion and intersystem crossing or intramolecular charge transfer (see Figure 2, processes corresponding to τ_1 and τ_2). The coordination geometry, oxidation state, and spin state determine the 3d electron configurations, which are directly related to reactivity of the molecules. Thus, both intermediate states resulting from energy or charge transfer to the Ni center are catalytically relevant given the change in the electronic configuration at the Ni center. The information gathered from studying these molecules could, therefore, have broader impact for understanding the excited states of transition-metal-complex catalysts.

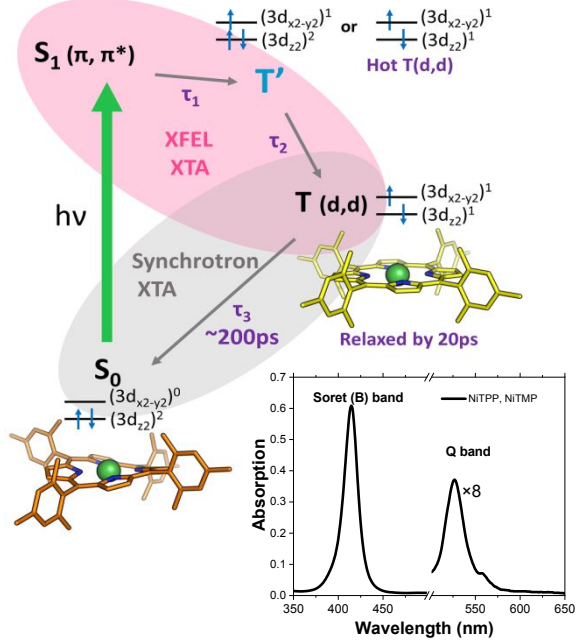

Figure 2. The relaxation pathway of NiTMP following Q-band excitation (527 nm shown in UV-vis in the bottom right). Specific relaxation pathways are highlighted to indicate the role that different X-ray facilities have in studying the excited-state dynamics of transition metal complexes. Structures and Ni electronic configurations of states characterized by XTA are shown. Diagram reprinted with permission from *J. Am. Chem. Soc.*, 2016, **138**, 8752. Copyright 2016 American Chemical Society.

A schematic description of the photoexcitation pathways of Ni(II) tetramesitylporphyrin (NiTMP) is shown in Figure 2.[69, 71, 72] As for most metalloporphyrins, photoexcitation at either the B (S_2 ← S_0 transition) or Q (S_1 ← S_0 transition) bands of NiTMP induces a π-π* transition in the macrocycle, promoting an

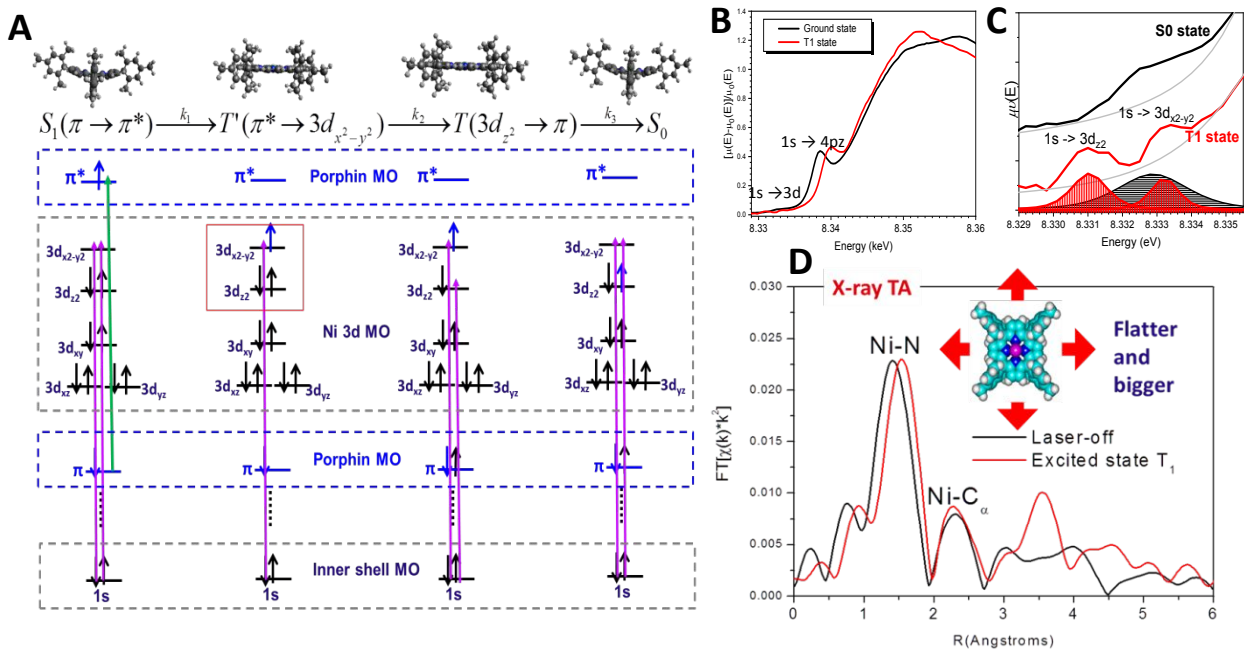

Figure 3. A) Calculated structures of different states, sequential kinetics schedule, electronic configurations, and visible (green vertical arrow) and X-ray (purple vertical arrows) induced transitions; B) Ni K-edge XANES spectra of the ground (S_0) and T_1 states, obtained by 100 ps X-ray probe pulses from the Advanced Photon Source; C) pre-edge region of the Ni K-edge XANES; and D) EXAFS spectra of the S_0 and T_1 states. Adapted from Ref. 72 (B, C) and Ref. 75 (D).

electron to the π* orbital and leaving a hole in the π orbital.[73] The pump-probe and pump-pump-probe OTA measurements of analogous Ni(II) tetraphenylporphyrin (NiTPP) suggested that the extra electron in the π* orbital subsequently transfers to the vacant $3d_{x2-y2}$, while the hole in the π-orbital would be filled by one of the $3d_{z2}$ electrons.[74] This can occur sequentially, generating a transient Ni(I) center with electronic configuration indicated by the left diagram for the T' state in Figure 2, or in a concerted manner, generating an excited Ni (*d,d*) state with the electronic configuration indicated by the right diagram for the T' state. Regardless, in less than 20 ps, the Ni(II)TPP ligand-centered excited state transforms to the T_1 state with singly occupied $3d_{x2-y2}$ and $3d_{z2}$ orbitals,[75] which then decays with a time constant of ~200 ps in toluene. The OTA results for NiTMP are almost the same as those of NiTPP. However, the results from the OTA measurements alone could not directly verify the electronic configuration in terms of the *d*-orbital occupation and the energy gaps between the vacant orbitals. Ni(II) has a square-planar $3d^8$ ($3d_{xy}^2$, $3d_{xz}^2$, $3d_{yz}^2$, $3d_{z2}^2$, $3d_{x2-y2}^0$) electronic configuration in the ground state S_0 (Figure 2). Moving forward we will only indicate the empty or partially filled orbitals—($3d_{x2-y2}^0$) for the NiTMP S_0 state. In the absence of ligating solvent molecules, the Ni(II) ($3d^8$) in the ground-state NiTMP has a vacant $3d_{x2-y2}$ orbital (Figure 2).

The calculated energy levels and structures for the states involved in the reaction pathways are shown in Figure 3A. These calculations raise the following questions: 1) what are the excited-state trajectories in terms of both electronic and nuclear structural changes, and 2) what structural factors modulate the excited-state pathways and dynamics. XANES spectra are sensitive to electronic configurations of transition metal elements, especially for the 3*d* elements. The pre-edge region of the XANES spectrum features the dipole-forbidden, quadrupole-allowed 1s to 3d transitions when there are vacancies in the 3*d* orbitals, with transition intensities sensitive to the *d-p* mixing and thus indicative of the 3*d* orbital occupation and coordination geometry. Figure 3B shows the XANES spectra for the ground (S_0) and thermally equilibrated T_1 state ~100 ps after excitation of the porphyrin ligand-centered π → π* transition. As it is typical for a square-planar coordination geometry of Ni(II) ($3d^8$) in the ground state, the only empty 3*d* orbital is $3d_{x2-y2}$, so there is only one quadrupole-allowed 1s to 3d transition peak observed in the pre-edge region (Figure 3C). XTA spectra were obtained by using X-ray probe pulses from a synchrotron source (the Advanced Photon Source, Argonne National Laboratory) with ~100 ps time resolution; two pre-edge peaks are observed, indicative of the T_1 state, at the Ni K-edge with ~200 ps lifetime (Figure 3C). The two peaks correspond to the changes in the 3*d* orbital occupancy in the T_1 state. After excitation with 527 nm light, an electron from the π-π* transition transfers to the empty $3d_{x2-y2}$ orbital and an electron from the filled $3d_{z2}$ orbital fills the hole of the transient singly occupied π orbital. With the two highest energy 3*d* orbitals, $3d_{x2-y2}$ and $3d_{z2}$, only singly occupied, two possible 1*s* to 3*d* transition pre-edge features are observed corresponding to respective transitions to each orbital. Thus, the XANES results verified that the electronic configuration of the thermalized excited T_1 state has a ($3d_{x2-y2}^1$, $3d_{z2}^1$) electronic configuration (the T(*d,d*) state in Figure 2).

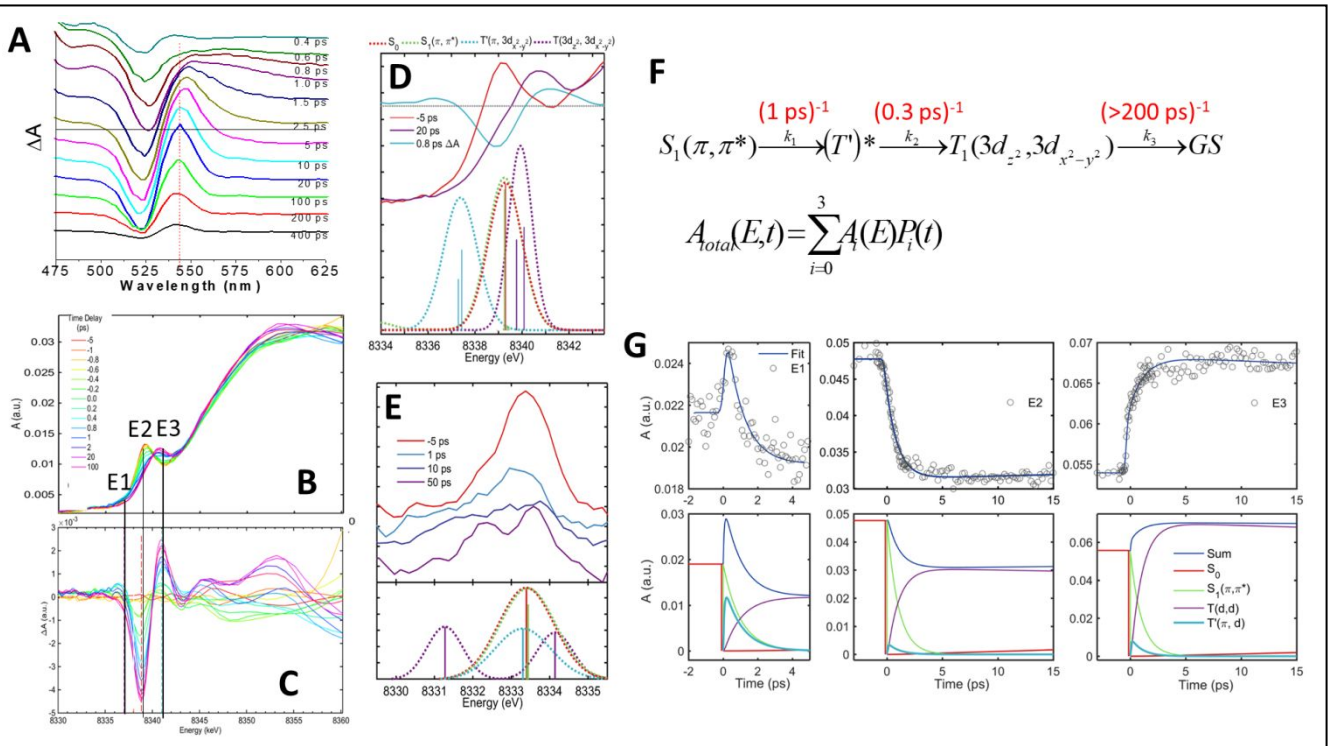

Figure 4. A). OTA measurement of NiTMP in toluene; B) Ni K-edge XANES spectra and C) difference spectra measured with femtosecond X-ray pulses; D) calculated 1s →4p_z transition features (lower panel) and the corresponding difference signal for the T' state (cyan, top panel); E) observed (top) and calculated pre-edge 1s →3d transitions for the indicated states in the legend in D; F) schematic of the sequential kinetic model and equation used to fit kinetic traces at indicated probe energies; G) decomposition of the simulated kinetic trace into the signal amplitude for each species as described by the equation in F). B, C, D, E, G adapted with permission from *J. Am. Chem. Soc.*, 2016, **138**, 8752. Copyright 2016 American Chemical Society.

Distinct peaks at 8339 eV in the S_0 state spectrum and at 8341 eV in the T(*d,d*) state spectrum (Figure 3B) are assigned to the strong dipole-allowed 1s→ 4p_z transitions.[76] Features near the white-line absorption peak (the most intense feature in the XANES spectra) at 8351 eV are assigned as contributions from multiple scattering resonances (where the photoelectron scatters off several neighboring atoms sequentially) and transitions from Ni 1s to σ* antibonding molecular orbitals resulting from the hybridization of Ni 4p_x and 4p_y orbitals with porphyrin N 2*s* orbitals. Similar to the 3d_{x2-y2} being higher in energy than the 3d_{z2} orbital, the 4$p_{x,y}$ orbitals are higher in energy than the 4p_z orbital due to the strong sigma interactions with the porphyrin macrocycle. The 4*p* orbitals are vacant for Ni complexes, so changes in transition energies to these orbitals, as well as to all high energy bound states, are determined by perturbations to the 4p energies and changes in the energy of the core orbitals due to structural or oxidation state changes.

Meanwhile, the Ni(II) coordination geometry in the excited-state NiTMP was also extracted from the XTA results showing ~0.08 Å longer Ni-N and Ni-C_α (C_α atoms are two carbon atoms connected directly to the N atom ligated with Ni) distances than those in the ground state (Figure 3D).[75] Such increases can be understood as macrocycle expansion due to a decrease in the Ni-N bond order from the addition of an electron to a more energetically destabilizing 3d_{x2-y2} orbital in the excited state, which results in higher antibonding character in the Ni-N bond. Consequently, the Ni(II) radius in the new electronic configuration in the T_1 state is effectively larger than that in the ground state as shown by the 0.08 Å elongation of the Ni-N bond. These XTA measurements of Ni(II) porphyrin demonstrate the utility of XTA in providing simultaneous transient electronic and structural information regarding the metal center, providing the impetus for similar experiments that have become common at synchrotron light sources.

However, the limitation of ~100 ps time resolution provided by the X-ray pulses from synchrotron sources precludes detection of the sub-picosecond component observed in the OTA measurements (Figures 2 & 4). Further, the time sequence of the electron migration from initially populated π* orbital to the empty 3d_{x2-y2} and then one 3d_{z2} electron moving to fill the hole in the π-orbital created by the photoexcitation was also unclear. Particularly, it is important to know if a transient Ni(I) species is present, and, if so, how its lifetime could be controlled for potential catalytic applications.

In order to capture the ultrafast electronic structural evolution during the early time of the excited-state trajectory, an XTA study of NiTMP in solution was carried out with femtosecond X-ray pulses provided by the hard X-ray free electron laser (XFEL), Linac Coherence Light Source (LCLS). Unlike synchrotron sources, the XFEL source used self-amplified spontaneous emission, which is capable of generating intense pulses with temporal widths shorter than 100 fs, but with

limited energy span, i.e. ~30-40 eV. The final timing and energy dependent signal intensities are sorted out with a data extraction program developed by the facility for the users. More recently, the facility has improved its capability of carrying out EXAFS data collection,[77, 78] which opens opportunities in femtosecond nuclear structural determination in transition metal complexes.

The OTA results of NiTMP shown in Figure 4A suggested a three-exponential fit to the excited state kinetics with time constants of 0.2-0.4 ps, 10-20 ps and ~200 ps. In the XTA results shown in Figures 4B & 4C,[69] there are three characteristic energy points, E1, E2 and E3, at which the most intense difference XANES signals were observed. The features at E2 and E3 were observed in the synchrotron experiments shown in Figure 3, and correspond to the bleach of the ground-state S_0 1s → $4p_z$ transition and induced absorption of the transient T_1 state 1s → $4p_z$ transition. The most surprising results in this spectral region can be seen in Figure 4C, where a feature in the difference signal emerged transiently at E1 that was not observed in the synchrotron measurements. The E1 feature rises rapidly to its maximum amplitude at 400 - 800 fs, and decays within ~2 ps (Figures 4C & 4G).

Quantum mechanical calculations of the inner shell transitions were performed to identity the feature at E1 for the relevant states (Figure 4D,E) involved in the sequential kinetics equation in Figure 4F. The T′ state in the calculation has an electronic configuration of Ni(I) ($3d_{x2-y2}^1$, $3d_{z2}^2$), formed when the electron from the initially populated π* orbital migrated via intramolecular charge transfer to fill a vacancy in the $3d_{x2-y2}$ orbital. Since the $(3d_{z2})^2$ orbital remained doubly occupied, a transient Ni(I) was formed in the T′ state. The calculations revealed that the $1s \rightarrow 4p_z$ transition for the T′, S_0 and T_1 states appeared in the same energetic order as observed experimentally. The lowest energy 1s → $4p_z$ transition of the T′ state arose from the transient Ni(I) ($3d_{x2-y2}^1$, $3d_{z2}^2$) configuration, with an ~2 eV decrease in the energy gap relative to the S_0 state. This is consistent with general trends, where lower oxidation states for a given metal require less energy to remove an electron from the core. The charge-transfer state, with (π, $3d_{x2-y2}$) orbital character, likely induced intersystem crossing because 1) the charge-transfer process involved a change in orbital angular momentum (π*→$3d_{x2-y2}$), 2) the ^{1}(π, $3d_{x2-y2}$) and ^{3}(π, $3d_{x2-y2}$) states have similar energies, and 3) enhanced spin-orbit coupling due to increased electron density on the Ni center.[69]

Based on the calculated Ni K-edge transition energies and the observed transient XANES features of corresponding electronic states, a global analysis of the spectral and temporal XTA signals at E1, E2 and E3 using the expression of $A_{total}(E,t)$ was performed using a sequential kinetics model as outlined in Figure 4F, where *i* is the index of the states, *i* = 0 - 3, corresponding to S_1(π, π*), T′, T_1, and S_0 states, $A_i(E)$ is the relative absorption of the *i*-th state at E, and $P_i(t)$ is the population of *i*-th state at *t*. The kinetics fitting revealed time constants of 1 ps, 0.3 ps, and >200 ps for the three-step sequential model (Figure 4F). The sub-picosecond time component was also detected in OTA, while the two longer time components with time constants of 20-ps observed in OTA were not extracted in the XTA data due to the limited experimental time window. The assignment of these time constants to specific processes required the relative absorption properties of each state involved. This was determined with the assignment of the difference XANES spectral feature at E1 to the 1s → $4p_z$ transition peak of the T′ state (Figure 4G).[69] The decomposition of the total signal (Figure 4G) shows that the apparently faster rise at E2 compared to the decay at E1 arises from a small positive contribution to the signal from T′ at both energies that rises and decays quickly. The dynamics of the T′ state exhibit inverted kinetics, with a rise time of 1 ps and decay time of 0.3 ps. The 1 ps rise of the T′ population reflects the 1 ps decay of the S_1(π, π*) population from which T′ is being generated, while the <0.3 ps decay of the T′ state limits accumulation of T′ population, even when the initial population of S_1(π, π*) is large. As a result, the population and rise time of the T(d,d) state closely follows the rate of formation of this intermediate state, as this is essentially rate limiting. The population kinetics follow our observation that the transient T′ state is only detectable for 1-2 ps.

The T′ and T_1 excited-state NiTMP structures calculated by DFT feature progressive increases of the Ni-N bond distance and transformation from a non-planer ground-state macrocyclic conformation to more planar conformation.[40, 69, 75] The combined structural results from X-ray sources and DFT calculation showed structural changes such as macrocycle expansion in the excited states. The influence of the porphyrin macrocycle conformation on the relaxation kinetics—through σ interactions that affect the $3d_{x2-y2}$ orbital energy—may be significant enough to affect the kinetics that govern the limited population accumulation of the transient Ni(I) state. The short lifetime of the T′ state and the delay of the nuclear rearrangement to a longer Ni-N bond length and flattened macrocycle with respect to its formation suggests the still-ruffled macrocycle expedites T′ decay. Thus, one can rationalize the structures that favor the transient Ni(I) in the T′ state based on the structural dynamics extracted from both XTA and the DFT-optimized geometries on the hundreds of picosecond to sub-nanosecond time scales. Other XTA studies on Ni(II) porphyrins have further addressed the importance of structural effects by constraining the planarity of the macrocycle and the impacts on the structural dynamics of the excited state.[79] The studies on Ni(II) phthalocyanine aimed at investigating such effects will be discussed in Sections 4-6.

3. Structural Dynamics of Axial Ligation of Nickel Porphyrin in the Ground and Excited States

One of the most important chemical processes in transition metal complexes is the ligation and deligation of solvents or other small molecules to and from the metal center, corresponding to metal-ligand bond formation and breakage. These events are determined not only by thermodynamic energies of ligated and unligated species, but also by the structural dynamics of the molecules under consideration. Here

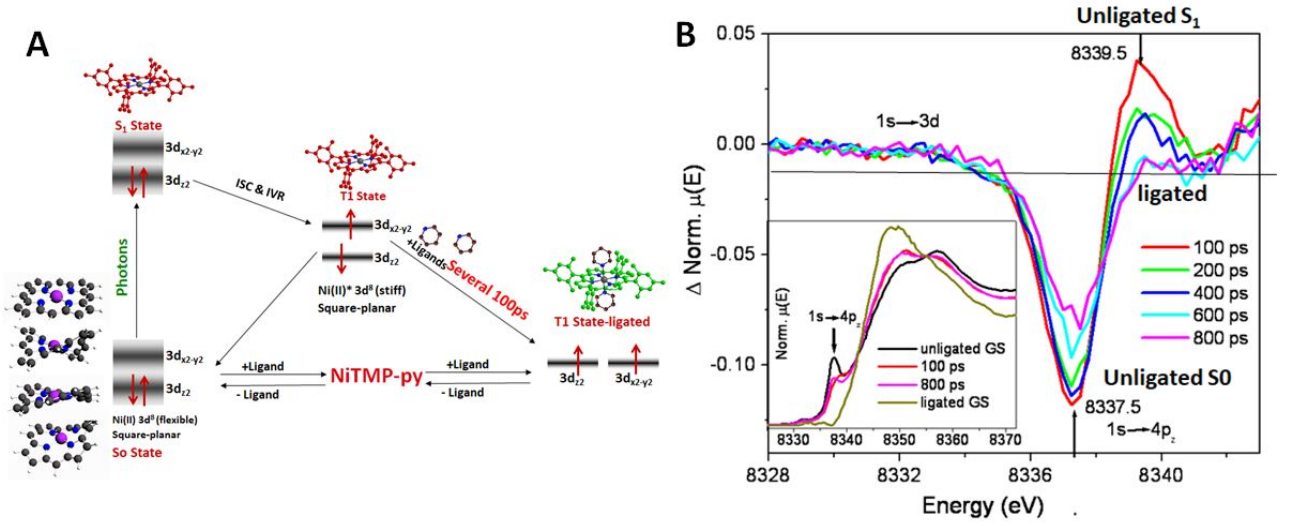

Figure 5. A) A unified ligation mechanism of photoexcited NiTMP; B) 1s →4p$_z$ transition region as a function of the pump-probe delay time in XANES spectra (inset) taken in a mixed solvent (25% pyridine, 75% toluene by volume). B reproduced from Ref. 72 with permission from the Royal Society of Chemistry.

two examples are given for the ligation and deligation from metalloporphyrins, respectively.

Severe out-of-plane distortions for Ni(II) porphyrins have been found in the ground state with domed, saddled, twisted and butterfly-like distortions.[80, 81] The 1s → 3d$_{x2-y2}$ transition in the unligated, ground-state NiTMP was observed to have a peak width (full-width half-maximum, FWHM) greater than 2 eV, while the 1s → 3d$_{z2}$ and 1s → 3d$_{x2-y2}$ transitions in the excited T_1 state had peak widths of about 1.2 eV (Figure 3C).[72] Assuming the 1.2 eV peak width is due to the instrumentation-limited energy resolution, then the broader peak width of 2 eV is indicative of the 1s → 3d_{x2-y2} energy distribution in the ground state arising from 3d$_{x2-y2}$ orbital energies among the conformers, which is larger than the energy resolution of the instrumentation, and much larger than kT (0.025 eV at room temperature). This agrees with the DFT calculations on different conformers of NiTMP[72] where the corresponding energies for 3d$_{x2-y2}$ and 3d$_{z2}$ orbitals can differ by more than 1 eV between the conformers. These changes in the 3d$_{x2-y2}$ orbital energies will lead to transitions at different energies for each conformer. However, the observation of a single Gaussian peak broader than the range of calculated 3d$_{x2-y2}$ energies indicates that the individual conformers cannot be resolved. Additionally, the large variation in 3d$_{x2-y2}$ and 3d$_{z2}$ orbital energies may be offset by the solvent interactions of the different conformers, which could keep the total energies (conformer and solvent) within kT at room temperature.[72]

This broad distribution of 1*s* → 3d_{x2-y2} transition energies could have a profound effect in the axial ligation of metalloporphyrins. Previous OTA studies revealed that the excited-state Ni porphyrin tends to ligate with different Lewis base solvents with lone pair electrons from N or O in the axial direction.[82, 83] Axial ligation direction aligns with the 3d_{z2} orbital, so its electron occupation strongly influences reaction dynamics. A partially to completely vacant 3d_{z2} will stabilize the lone pair electrons from the N or O atom in the Lewis basic ligand more favorably than a fully occupied 3d_{z2}. Our calculations indicated that the energy gap between the 3d_{z2} and 3d_{x2-y2} orbitals can also change by up to 1 eV, ranging between 1.1 and 2.2 eV for the selected conformer structures.[72] Transient interactions between free Lewis basic ligands and ground state NiTMP could destabilize the 3d_{z2} orbital, further decreasing the energy gap between the 3d_{z2} and 3d_{x2-y2} orbitals. It is possible that combined effects from the conformers and solvent interactions bring the 3d_{z2} and 3d_{x2-y2} orbitals in transient degeneracy, enabling electron hopping from the filled 3d_{z2} to empty 3d_{x2-y2} orbitals. The partially filled 3d_{z2} would then further promote formal ligation of the ground state NiTMP. This nuclear structural influence on the orbital energy levels will also provide guidance in synthesizing metalloporphyrins with desirable out-of-plane distortions that modulate the energy levels of the d orbitals to promote particular photochemical reactions.

In the presence of ligating molecules in solution, e.g., pyridine, Ni(II) porphyrins undergo axial ligation in the ground state and photoinduced axial ligation/deligation in the excited states[84, 85]. The questions then are 1) what is the driving force for the empty 3d_{x2-y2} and the occupied 3d_{z2} orbitals of the starting Ni(II) porphyrin to allow the axial ligation, and 2) what is the time sequence for ligation with respect to the electronic configuration change? These questions are important for our understanding of the correlations between electronic and nuclear structures of the molecule, as well as controlling molecular reactivity through structural modification. In the presence of ligating pyridine in solution, OTA measurements following the 527 nm excitation (i.e., only unligated species is excited by photons at this wavelength) obtained the ground-state recovery kinetics described by the sum of three exponential functions with the decay time constants, τ_1 = 20 ps, τ_2 = 255 ps, and τ_3 = 42 ns. These time constants correspond to

the processes of intramolecular vibrational relaxation and vibrational cooling, branched evolution to a long-lived ligated excited state or back to the ground state, and, lastly, deligation of the doubly ligated species.[71, 83]

The excited-state axial ligation can be monitored by XTA via the $1s \rightarrow 4p_z$ transition feature at 8337.5 eV of the Ni K-edge (Figure 5B).[86-88] This $1s \rightarrow 4p_z$ feature is the most pronounced in the square-planar geometry with no axial ligand, and the peak energy of this feature progressively moves to higher energies as the metal center binds one or two axial ligands.[40, 89, 90] The almost completely doubly ligated hexa-coordinated Ni(II) in NiTMP (Figure 5B) has no visible $1s \rightarrow 4p_z$ feature at 8337.5 eV because the corresponding transition energy is now degenerate with the $1s \rightarrow 4p_{x,y}$ transitions and has merged with the white-line feature at 8345-8350 eV.[40] Therefore, the peak intensity at 8337.5 eV is entirely from the unligated species, which can be used to monitor the ligation dynamics in the XANES region.

Because a dual-ligated NiTMP has no $1s \rightarrow 4p_z$ feature in the middle of the rising Ni K-edge,[76, 86] if NiTMP forms a penta- or hexa-coordinated species after the photoexcitation, we should see a decrease in the sharp $1s \rightarrow 4p_z$ peak at 8337.5 eV. Instead, we observed that the $1s \rightarrow 4p_z$ transition peak intensity of NiTMP in the mixed solvent did not decrease at 100 ps after the photoexcitation, but shifted to a higher energy (Figure 5B, and inset). This is very similar to that for the T_1 state of NiTMP in toluene where the axial ligation does not occur.[75] During the 100 to 400 ps pump-probe delays, the intensity at 8339.5 eV reduced in the transient difference spectra in Figure 5B and decays almost completely by 600 ps as the unligated NiTMP population decreased. By 600 - 800 ps time delays, the $1s \rightarrow 4p_z$ peak at 8337.5 eV has reappeared, but with reduced intensity. Because the dual ligated NiTMP has a higher energy $1s \rightarrow 4p_z$ peak merged with the white-line peak, it will not contribute to the intensity at 8337.5 eV nor be resolved from the white-line feature. Therefore, the reduced intensity at 8337.5 eV and absence of new features on the Ni K-edge indicates that dual ligation has occurred. The slow decay of the ground-state bleach of the unligated $1s \rightarrow 4p_z$ transition at 8337.5 shows the photoinduced-ligated NiTMP decays to the ground state with a time constant of 42 ns. From these XTA results, one can map out the population of the ground-state unligated, ground-state ligated, and excited-state unligated complexes as a function of the delay time, which provides new insight into the details of NiTMP ligation dynamics in addition to what was observed by OTA spectroscopy.

The XTA studies on the photoexcited NiTMP revealed a unified mechanism for the ground-state and photoinduced ligation. Photoexcitation of the Q band created vibrationally excited, singly-occupied $3d_{z2}$ and $3d_{x2-y2}$ orbitals that favor axial ligation. However, axial ligation with the excited-state NiTMP does not occur immediately, but is a diffusion-limited process. The study outlined a unified mechanism for axial ligation driven by the vacancy in the $3d_{z2}$ orbital in both ground- and excited-state NiTMP, which may be applicable to other metalloporphyrins. The dynamic 3*d* orbital energy distribution is expected to have a general impact in designing photocatalysts for promoting binding to the metal center in a well-defined orientation to achieve desirable products.

4. Ground-State Electronic and Structural Factors in Nickel Phthalocyanines

Phthalocyanines are structurally similar to porphyrins with four isoindole units connected via aza-bridges replacing the four pyrrole units and methine-bridges in porphyrins. Figure 6 depicts the structures of the various nickel(II) phthalocyanine (NiPc) complexes discussed here along with the optical absorbance spectra for a subset of these NiPc derivatives. The two structural differences between phthalocyanines and porphyrins are highlighted in magenta and cyan in Figure 6A. The replacement of pyrrole with isoindole leads to a larger aromatic system, decreasing the transition energy of the Q bands in the visible region of the electromagnetic spectrum.[91-93] From a solar photovoltaic and photochemical perspective, the shift of the absorbance spectrum to lower energies is advantageous for utilizing lower energy portions of the solar spectrum. Motivated by (1) the light absorption properties of metallophthalocyanines, (2) the structural disorder observed in ground-state NiTMP,[72] and (3) the observation of the transient Ni(I) intermediate in NiTPP[69] and indications of long-lived Ni(I) states in NiPc-$^{\alpha}$OBu,[94, 95] we used XTA spectroscopy to investigate the excited-state dynamics of NiPc-$^{\alpha}$OBu.

Prior systematic investigations demonstrated the effect of varying the substituent pattern on the absorbance spectra of metallophthalocyanines[96-98]—one example using ZnPc-OBu complexes as models is given in Figure 6B. These studies with ZnPc complexes, using butoxy (OBu) and phenyl groups, demonstrate that bulky R_1 substituents shift the Q band to a lower energy (longer wavelength). These butoxy-substituted zinc(II) phthalocyanine complexes, along with butoxy-substituted nickel(II) phthalocyanine complexes, show that the electron donating/withdrawing character of R_1 and R_2 and the bulkiness of R_2, however, have minimal effects on the Q-band energy. The dependence of the Q-band energy on the bulkiness of R_1 and lack of dependence on R_2 indicates that structural distortion of the phthalocyanine skeleton away from planarity is primarily responsible for shifting the Q band to lower energy. Indeed, DFT studies and crystal structures reveal a saddled phthalocyanine skeleton for NiPc-$^{\alpha}$OBu[94] with R_1 = OBu and R_2 = H and a nearly planar phthalocyanine skeleton for NiPc-H[99] and NiPc-$^{\beta}$OBu[100] with R_1 = H and R_2 = OBu.

The phthalocyanine cavity is smaller than the porphyrin cavity, showing, on average, 0.05 Å shorter metal–nitrogen bonds and 3° smaller aza-bridge bond angles than methine-bridge bond angles.[93] The decrease in the aza-bridge bond angle was attributed to electron repulsion from the lone pairs of the nitrogen atom in the aza-bridge. The smaller bond angles result in a smaller cavity in phthalocyanine, compared to porphyrin, which is better suited to bind the small Ni(II) ion. The improved ability of phthalocyanine to accommodate Ni(II) is clearly observed by comparing the width of the pre-edge peaks in XANES spectra measured at the Ni K-edge for NiTMP (Figure 3C)

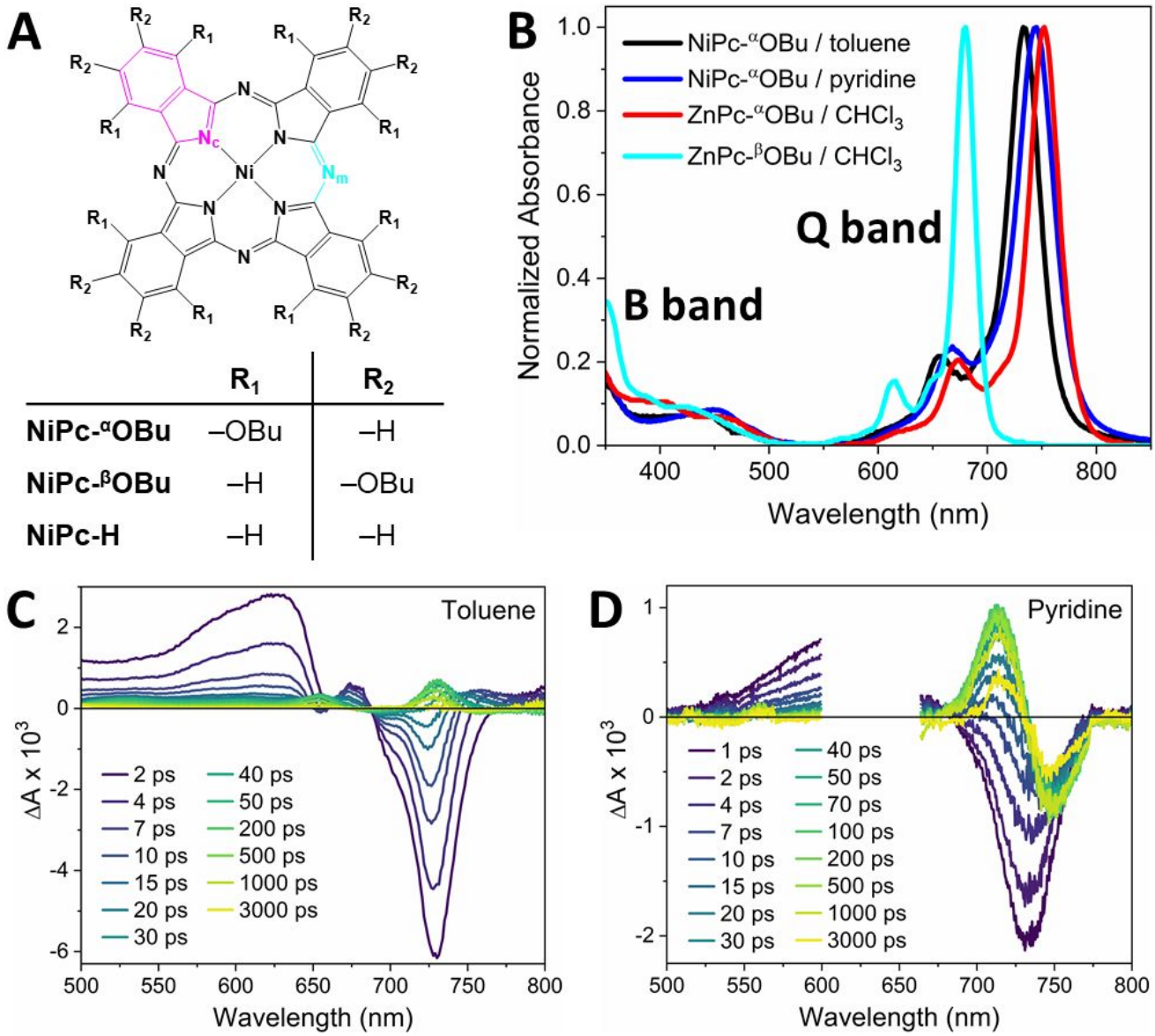

	R_1	R_2
NiPc-αOBu	–OBu	–H
NiPc-βOBu	–H	–OBu
NiPc-H	–H	–H

Figure 6. Structure and optical absorbance spectra of NiPc complexes. (A) Structures of NiPc complexes discussed here. (B) Optical absorbance spectra of NiPc-αOBu in non-coordinating and coordinating solvents and of ZnPc-αOBu and ZnPc-βOBu in chloroform. Optical transient absorption spectra for solutions of NiPc-αOBu in (C) toluene following excitation at 415 nm and (D) pyridine following excitation at 640 nm. ZnPc-α/βOBu absorbance spectra in B digitized from Ref. 98 (https://doi.org/10.1021/acsomega.8b03500), future permission requests should be directed to the American Chemical Society. C adapted from *ChemSusChem*, 2018, **11**, 2421 with permission (copyright 2018 Wiley-VCH Verlag GmbH &Co. KGaA, Weinheim). D reprinted from *J. Photoch. Photobio. A*, Vol. 372, Jiyun Hong, Thomas J. Fauvell, Waleed Helweh, Xiaoyi Zhang, Lin Chen, Investigation of the photoinduced axial ligation process in the excited state of nickel(II) phthalocyanine, pp. 270-278, Copyright (2019), with permission from Elsevier.

and NiPc-αOBu (Figure 7B). The FWHM of the pre-edge feature in NiPc-αOBu, centered around 8333 eV, was observed to be about 1.6 eV, only about two-thirds the >2 eV FWHM of the measured NiTMP pre-edge feature.[72, 101]

Different phthalocyanine conformations result in varied degrees of mixing between the Ni $3d_{x2-y2}$ orbital and Pc-based ligand orbitals, leading to a distribution of Ni $3d_{x2-y2}$ energies. The narrower width of the measured pre-edge feature in NiPc-αOBu indicates that there are fewer conformations of NiPc-αOBu present in solution at room temperature than in NiTMP. As discussed earlier, NiPc-αOBu adopts a saddled phthalocyanine skeletal structure to minimize steric interactions between the R_1 = OBu substituents.[94] The pre-edge feature intensity should be sensitive to phthalocyanine skeletal distortions, like the saddled structure of NiPc-αOBu, that reduce centrosymmetry. However, mixing between the 4*p* and $3d_{x2-y2}$ orbitals is symmetry-forbidden in both the D_{2d} and D_{4h} point groups. Thus, the energy and width, but not the intensity, of the Ni $3d_{x2-y2}$ pre-edge transition are characteristic markers for the

type and number of phthalocyanine, and porphyrin, conformers.

X-ray absorption spectra measured at the Ni L3-edge probe dipole-allowed Ni $2p \rightarrow 3d,4s$ transitions (Figure 7F), providing increased sensitivity to the bonding interactions between the Ni and phthalocyanine ligand.[102] The Ni L3-edge spectra in both NiPc and various nickel porphyrin (NiP) complexes are characterized by an intense absorption corresponding to the Ni $2p_{3/2} \rightarrow 3d_{x2-y2}$ transition (labeled A) with satellite features corresponding to transitions from Ni $2p_{3/2}$ orbitals to molecular orbitals with mixed Ni 3*d*, 4*s* and N 2*p* character (labeled A_2, A_3, C, C*, and D). The intense Ni $2p_{3/2} \rightarrow 3d_{x2-y2}$ transition in NiPc is higher in energy than that of the NiP complexes, reflecting decreased Ni 3*d* electron density due to increased π-back-bonding and stronger Ni–N covalent interactions. The Ni L3-edge spectra were used to correlate the magnitude of the saddle distortion and the skeletal composition—nitrogen vs carbon atoms in the meso positions—with the number, energy, and width of the satellite features since they directly probe the molecular orbitals with mixed Ni and ligand character.

5. Electronic and Structural Character of the Longest-Lived Nickel Phthalocyanine Transient State

Millard and Greene first reported the OTA spectroscopy and excited-state dynamics for NiPc-H in 1985,[103] while Rodgers et al followed for NiPc-H and NiPc-$^{\alpha}$OBu in 2005[94] and 2007[99] and Pfleger et al followed for NiPc-$^{\beta}$OBu in 2014.[100] Spiro et al then followed with time-resolved femtosecond Raman-induced Kerr effect spectroscopy (FRIKES) measurements on NiPc-$^{\alpha}$OBu in 2014.[95] These measurements revealed similar temporal dynamics for the measured NiPc complexes as those observed in NiP complexes, but were interpreted differently depending on the identity of the R_1 and R_2 substituents.

The OTA measurements on solutions of each of the NiPc complexes in non-coordinating solvents reveal three principal kinetic components. Figure 6C provides example OTA spectra measured on solutions of NiPc-$^{\alpha}$OBu in toluene.[101, 104] Two features dominate the transient spectra immediately following excitation of the Q band: first, an intense negative feature due to bleaching of the ground-state absorption along with stimulated emission from S_1 to S_0 and, second, a positive feature between 550-650 nm due to absorbance from S_1 to higher-lying excited states. These features decrease in amplitude during the first 10 ps as a new feature with positive absorbance appears on the low energy side of the ground-state bleach. The new positive feature shifts to higher energies during the first 50 ps after excitation. In NiPc-$^{\alpha}$OBu, which adopts the saddled conformation, the terminal transient state exhibits a second-

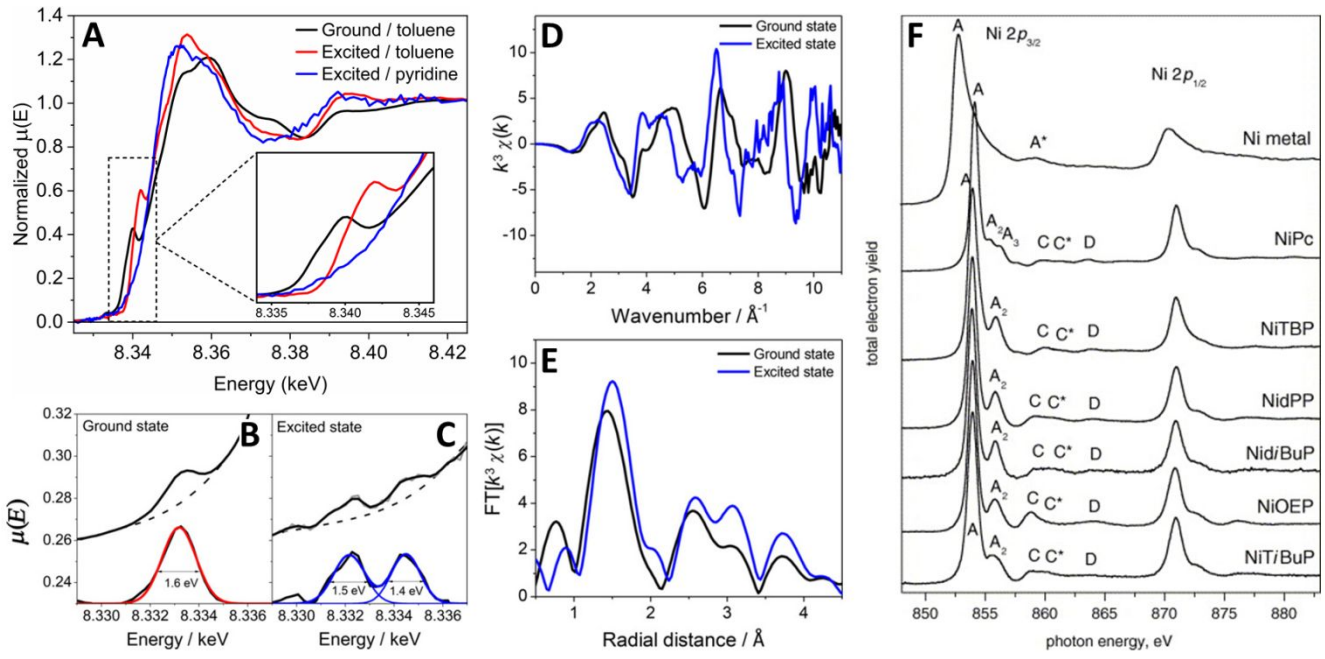

Figure 7. X-ray absorption spectra of NiPc complexes. (A) XANES spectra at Ni K-edge for a solution of NiPc-$^{\alpha}$OBu in toluene and pyridine with inset showing Ni $1s \rightarrow 4p_z$ feature. For a solution of NiPc-$^{\alpha}$OBu in toluene, the pre-edge region of the Ni K-edge in the (B) ground and (C) excited state and EXAFS spectra of the ground and excited states plotted in (D) k-space and (E) R-space. (F) X-ray absorption spectra at the Ni L3-edge for NiPc-H and several NiPor complexes. A adapted from Ref. 101 and Ref. 104. B, C, D, E reprinted from *ChemSusChem*, 2018, **11**, 2421 with permission (copyright 2018 Wiley-VCH Verlag GmbH &Co. KGaA, Weinheim). F reprinted from *Chem. Phys.*, Vol. 332, S. A. Krasnikov, A. B. Preobrajenski, N. N. Sergeeva, M. M. Brzhezinskaya, M. A. Nesterov, A. A. Cafolla, M. O. Senge, A. S. Vinogradov, Electronic structure of Ni(II) porphyrins and phthalocyanine studied by soft X-ray absorption spectroscopy, pp. 318-324, Copyright (2007), with permission from Elsevier.

derivative-like lineshape, indicative of a narrower and more intense Q band compared to that of the ground state. In contrast, NiPc complexes with planar conformations, like NiPc-H and NiPc-$^{\beta}$OBu exhibit a first-derivative-like lineshape in the terminal transient state,[99, 100] consistent with a lower energy Q band in the excited state than in the ground state.

The excited-state dynamics for NiPc-H and NiPc-$^{\alpha/\beta}$OBu were interpreted using the OTA and FRIKES spectra, TD-DFT calculations of the excited states, and simulated spectra,[94, 95, 99, 100, 103] though here we focus only on the longest-lived excited state since the faster dynamics are obscured by the about 100 ps time resolution available at synchrotron facilities. Rodgers et al identified the terminal transient state in NiPc-$^{\alpha}$OBu as the Ni(I)-Pc$^{\bullet+}$ charge-transfer 1^3A_2 state of $^3(\pi, 3d_{x2\text{-}y2}^1)$ character (D_{2d} point group) and not the Ni (d,d) 1^3B_2 state of $^3(3d_{z2}^1, 3d_{x2\text{-}y2}^1)$ character or Pc-centered 1^3E state of $^3(\pi, \pi^*)$ character.[94] The intermediate excited state preceding the terminal transient state was assigned as the $^3(3d_{z2}^1, 3d_{x2\text{-}y2}^1)$ state due to the first-derivative-like lineshape, while the $^3(\pi, \pi^*)$ state was discarded on the basis that the observed transient spectrum did not resemble that of $^3(\pi, \pi^*)$ states in other phthalocyanine molecules and metallophthalocyanine complexes. In contrast, the first-derivative-like lineshape of the terminal transient state in NiPc-H led to assignment as the $^3(3d_{z2}^1, 3d_{x2\text{-}y2}^1)$ state.[99] For NiPc-$^{\beta}$OBu, Pfleger et al assigned the terminal transient state, featuring a similar first-derivative-like lineshape as NiPc-H, to one of the $^3(3d_{z2}^1, 3d_{x2\text{-}y2}^1)$ or $^3(\pi, \pi^*)$ states,[100] leaning towards the $^3(\pi, \pi^*)$ state but noting that a clear assignment could not be reached on the basis of the OTA spectra alone.

While the $^3(\pi, 3d_{x2\text{-}y2}^1)$, $^3(3d_{z2}^1, 3d_{x2\text{-}y2}^1)$, and $^3(\pi, \pi^*)$ states may yield indiscernible UV-vis absorption spectra, the different electronic character of the metal center for each state can yield clear differences in the corresponding X-ray absorption spectra. Indeed, calculated X-ray absorption spectra, referenced to that of the singlet ground state, indicated minimal changes for the $^3(\pi, \pi^*)$ state, while the $(3d_{z2}^1, 3d_{x2\text{-}y2}^1)$ state exhibited a splitting of the pre-edge feature and a shift of the Ni $1s \rightarrow 4p_z$ feature to higher energy.[101] The $^3(\pi, \pi^*)$ state has a similar X-ray absorption spectrum to the singlet ground state because the electronic transitions are localized on the ligand, while the Ni has the same oxidation state and electronic configuration. Similar to NiP complexes, the Ni pre-edge feature splits upon formation of the $(3d_{z2}^1, 3d_{x2\text{-}y2}^1)$ state due to a shift of the $1s \rightarrow 3d_{x2\text{-}y2}$ transition to higher energy and appearance of a new transition to the singly-occupied $3d_{z2}$ orbital at lower energy. Given the similarities between NiPc and NiP complexes,[72, 75, 101, 104] we assume the $(\pi, 3d_{x2\text{-}y2}^1)$ state of NiPc would also exhibit a lower energy Ni $1s \rightarrow 4p_z$ feature and less intense Ni $1s \rightarrow 3d_{x2\text{-}y2}$ feature.

The X-ray absorption spectra for the ground and excited states of NiPc-$^{\alpha}$OBu in non-coordinating solvents are provided in Figure 7A-C.[101] The excited-state spectra measured at 100 ps following excitation at 400 nm clearly show a shift of the Ni $1s \rightarrow 4p_z$ feature from 8340 to 8342 eV (Figure 7A), consistent with the predicted XANES spectra of the $(3d_{z2}^1, 3d_{x2\text{-}y2}^1)$ state. Additionally, higher resolution measurements at the pre-edge region for NiPc-$^{\alpha}$OBu show the splitting of the Ni $1s \rightarrow 3d_{x2\text{-}y2}$ feature (Figure 7B,C), providing further evidence that the terminal transient state is the $(3d_{z2}^1, 3d_{x2\text{-}y2}^1)$ state.

The XTA measurements on NiPc-$^{\alpha}$OBu reveal that the excited-state dynamics of the NiPc complexes are less sensitive to the bulkiness and electron-donating/withdrawing character of the R_1 and R_2 substituents than expected. The terminal excited states of NiPc-H and NiPc-$^{\alpha/\beta}$OBu were initially assigned to different electronic character based on differences in the OTA spectra and expected electron-donating effect of the OBu substituents. However, the Ni K-edge X-ray absorption spectra provide clear evidence of formation of the $(3d_{z2}^1, 3d_{x2\text{-}y2}^1)$ excited state, even in NiPc-$^{\alpha}$OBu. We note, however, that these measurements cannot rule out the presence of a short-lived charge-transfer state intermediate, similar to the Ni(I) transient state observed in NiTMP,[69] given the 100 ps time resolution. The XTA measurements and calculated XANES spectra for NiPc-$^{\alpha}$OBu further demonstrate the ability of XTA spectroscopy to differentiate and track many of the relevant intermediate states in photocatalytic reactions mechanisms.

The second-derivative-like lineshape in the OTA spectra of the $(3d_{z2}^1, 3d_{x2\text{-}y2}^1)$ excited state in NiPc-$^{\alpha}$OBu[94, 101] is anomalous compared to the first-derivative-like lineshape observed for the $(3d_{z2}^1, 3d_{x2\text{-}y2}^1)$ excited states in NiPc-H[99] and NiPc-$^{\beta}$OBu.[100] As Rodgers et al explained, the $(3d_{z2}^1, 3d_{x2\text{-}y2}^1)$ state results in only a minor perturbation to the phthalocyanine-based orbitals, which manifests as a small shift of the Q band to lower energy.[94] This perturbation in the Q band results in a transient difference spectrum with a first derivative-like lineshape centered near the ground-state Q band with negative absorption at higher energies and positive absorption at lower energies. As discussed above, the energy and width of the Q band depends primarily on the degree of phthalocyanine skeletal deformation, with larger deformations leading to larger shifts to lower energy.[96-98] If formation of the $(3d_{z2}^1, 3d_{x2\text{-}y2}^1)$ excited state in NiPc-$^{\alpha}$OBu resulted in increased planarity of the phthalocyanine skeleton, the Q band would shift to higher energy (shorter wavelength) than expected and decrease in width. These spectral changes could result in a second-derivative-like lineshape in the difference spectrum. Increased planarity of the phthalocyanine skeleton in the $(3d_{z2}^1, 3d_{x2\text{-}y2}^1)$ excited state in NiPc-$^{\alpha}$OBu is consistent with the phthalocyanine skeletal expansion indicated by the increased Ni–N_c and Ni–C_a bond lengths obtained from fitting the EXAFS spectra of the ground- and excited-state NiPc-$^{\alpha}$OBu.[101] These structural changes in the excited state are evident as increased frequency in the k-space EXAFS spectra and increased radial distance in the R-space EXAFS spectra (Figure 7D,E). Expansion of the phthalocyanine skeleton may relax the steric repulsion between the R_1 = OBu groups, enabling NiPc-$^{\alpha}$OBu to decrease the saddled distortion in the $(3d_{z2}^1, 3d_{x2\text{-}y2}^1)$ excited state.

While the OTA spectrum of the $(3d_{z2}^1, 3d_{x2\text{-}y2}^1)$ excited state of NiPc-$^{\alpha}$OBu indicates that the phthalocyanine skeleton adopts a more planar geometry in the $(3d_{z2}^1, 3d_{x2\text{-}y2}^1)$ state, the two observed pre-edge features have similar widths as the ground-state pre-edge feature. The similar widths of the ground- and excited-state pre-edge features in the Ni K-edge spectra indicate that there are a similar distribution of phthalocyanine

skeletal conformations in both the ground and excited state. This contrasts the decreased pre-edge peak width—and corresponding number of conformers present—in the ($3d_{z^2}^1$, $3d_{x^2-y^2}^1$) excited state of NiTMP.[72] This difference suggests that the skeletal distortions in NiP and NiPc complexes may result from different factors. The calculated ground-state structures of NiPc-H and NiPc-$^{\alpha/\beta}$OBu,[94, 99, 100] along with the narrow pre-edge feature in the X-ray absorption spectrum,[101] indicate that steric hindrance primarily between the R_1 substituents drives structural distortions in NiPc complexes. Since the steric hindrance of the substituents is decoupled from the electronic state of the NiPc complex, the distribution of conformers remains similar in the excited state. However, in NiP complexes, a larger mismatch between the size of the Ni(II) ion and the porphyrin cavity drives structural distortions. Thus, a smaller distribution of conformers is observed in the ($3d_{z^2}^1$, $3d_{x^2-y^2}^1$) excited state because the Ni–N bonds expand to better accommodate the size of the porphyrin cavity. These NiP and NiPc measurements provide insight on the interplay of ligand structure and substituents on the overall structural dynamics following excitation and illustrate how structural modifications to catalytic species could be interrogated and optimized.

In the photoexcited NiPc complexes discussed here, the R_1 and R_2 substituents do not appear to alter the sampled excited states, but they do affect the lifetime of the ($3d_{z^2}^1$, $3d_{x^2-y^2}^1$) excited state. The lifetime of the ($3d_{z^2}^1$, $3d_{x^2-y^2}^1$) excited states decrease in the order of NiPc-$^{\beta}$OBu (~820 ps) > NiPc-$^{\alpha}$OBu (~650 ps) > NiPc-H (~300 ps). This order of decreasing ($3d_{z^2}^1$, $3d_{x^2-y^2}^1$) excited-state lifetimes correlates with the electron-donating ability of the substituents. The OBu substituent is strongly electron donating, while the hydrogen groups have a neutral effect. The position of the substituent appears to have only a minor effect, if any, demonstrated by the about 820 ps and 650 ps ($3d_{z^2}^1$, $3d_{x^2-y^2}^1$) excited-state lifetimes of NiPc-$^{\beta}$OBu and NiPc-$^{\alpha}$OBu. This trend likely stems from inductive effects of the substituents on the Ni $3d_{x^2-y^2}$ orbital energy. The electron-donating OBu groups destabilized the $3d_{x^2-y^2}$ orbital in NiPc-$^{\alpha/\beta}$OBu more than in NiPc-H. The destabilized $3d_{x^2-y^2}$ orbital would have a larger energy gap between the $3d_{x^2-y^2}$ and $3d_{z^2}$ orbitals.[73] Thus, decay of the ($3d_{z^2}^1$, $3d_{x^2-y^2}^1$) excited state to the ($3d_{z^2}^2$, $3d_{x^2-y^2}^0$) ground state would occur more slowly in NiPc-$^{\alpha/\beta}$OBu than in NiPc-H.[105] Future studies may further explore the dependence of the excited-state lifetime on the electron-donating/withdrawing ability of the phthalocyanine substituents, along with pursuing XTA measurements with improved time resolution to understand better the excited-state relaxation dynamics.

6. Effect of Ligation on Excited-State Dynamics and Structure of Nickel Phthalocyanine

Excited-state ligation is a fundamental process in photocatalysis. Similar to NiP complexes, ligation was investigated in NiPc complexes given the open axial coordination sites and formation of the ($3d_{z^2}^1$, $3d_{x^2-y^2}^1$) excited-state, which is associative towards ligation. Figure 6A shows the

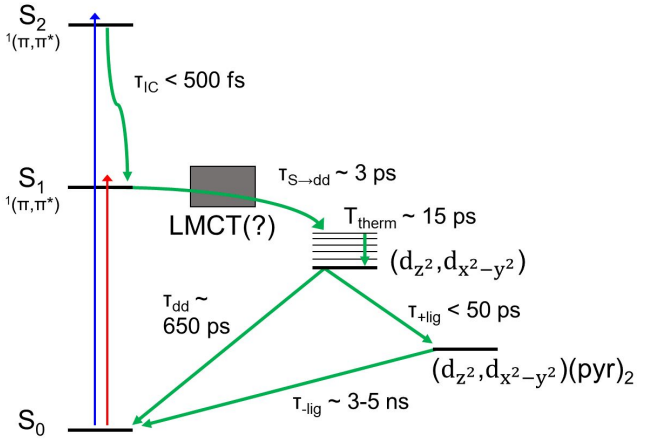

Figure 8. Jablonksi diagram summarizing the excited-state dynamics of NiPc-$^{\alpha}$OBu in both non-coordinating and coordinating solvents. Adapted from Ref. 101 and Ref. 104.

steady-state absorbance spectrum for a solution of NiPc-$^{\alpha}$OBu in pyridine, a common coordinating solvent. The absorbance spectrum for NiPc-$^{\alpha}$OBu in pyridine shifted to lower energy compared to that of NiPc-$^{\alpha}$OBu in toluene, but the change does not reflect the extensive differences seen for axially-ligated NiTMP complexes.[72, 106] The small shift in the visible absorbance spectrum when the solvent is changed from toluene to pyridine suggests that pyridine does not ligate NiPc-$^{\alpha}$OBu in the ground state. The tendency of NiPc-$^{\alpha}$OBu to exist in the unligated form in coordinating solvents stems from the structural differences of the phthalocyanine skeleton and the subsequent effect on the Ni 3*d* orbitals. The smaller cavity of the phthalocyanine skeleton,[93] compared to porphyrin, destabilizes the Ni $3d_{x^2-y^2}$ orbital due to increased overlap with the ligand sigma molecular orbitals. Since the six-coordinate ligated state favors the electron configuration ($3d_{z^2}^1$, $3d_{x^2-y^2}^1$), the destabilized $3d_{x^2-y^2}$ orbital precludes extensive ground-state ligation.

While ground-state NiPc complexes do not form six-coordinate ligated structures, the XTA spectra discussed above clearly demonstrate formation of the ($3d_{z^2}^1$, $3d_{x^2-y^2}^1$) state that promotes ligation. Indeed, OTA and XTA spectra of solutions of NiPc-$^{\alpha}$OBu in pyridine (Figure 6D and 7A, respectively) show clear differences from those measured for NiPc-$^{\alpha}$OBu in toluene.[104] The most striking difference in the XTA spectrum measured from 100 ps to 2 ns for NiPc-$^{\alpha}$OBu in pyridine is the missing Ni $1s \rightarrow 4p_z$ feature on the rising edge of the spectrum (Figure 7A and inset). The Ni $1s \rightarrow 4p_z$ feature likely shifted to higher energy due to interaction with the nitrogen lone pairs on the solvent molecules so that it became nearly degenerate with the $1s \rightarrow 4p_{x,y}$ transitions and merged with the white-line feature at about 8350 eV. The XANES spectrum of NiPc-$^{\alpha}$OBu in pyridine is qualitatively identical to that of ligated NiTMP discussed in section 2 (inset, Figure 5B).[72] Furthermore, the absent Ni $1s \rightarrow 4p_z$ feature in the 100 ps XTA spectrum indicates that excited-state ligation of NiPc-$^{\alpha}$OBu in pyridine completes within 100 ps.

The lack of the intense Ni 1*s* → 4p_z feature at 100 ps for NiPc-$^{\alpha}$OBu in pyridine provides clear evidence that nearly the entire excited-state population at 100 ps is ligated. Ligation must occur with a time constant less than 50 ps, possibly less than 20-30 ps, for the process to be nearly complete by 100 ps. These dynamics contrast the slower ligation process observed in NiP complexes. Even in pure pyridine, four-coordinate unligated NiP complexes undergo excited-state ligation on the hundreds of picoseconds timescale.[73, 107]

In the absence of ultrafast XTA measurements for the NiPc complexes, we use the OTA measurements to determine more precisely the ligation dynamics. The OTA spectra for NiPc-$^{\alpha}$OBu in pyridine appear similar to those in non-coordinating solvents during the first 1-2 ps (Figure 6D).[104] However, within 10 ps, the OTA spectra adopt a first-derivative-like lineshape, but with the positive absorption feature on the high-energy side of the Q band. The first-derivative-like lineshape near the Q band and weak absorption between 450 and 600 nm indicates that the transient state is again metal-centered, exerting only a small perturbation on the Pc-based Q band. The first-derivative-like lineshape increases in intensity with 10-20 ps, yielding the longest-lived transient state with about 2.5 ns lifetime.

Since the OTA spectra for NiPc complexes in coordinating solvents begin to differ from those in non-coordinating solvents as early as 5 ps, it seems that excited-state ligation of NiPc complexes occurs with a time constant less than 20 ps. Indeed, global kinetic analysis of the OTA spectra for NiPc-$^{\alpha}$OBu in pyridine yielded three kinetic processes with time constants of nearly identical to those measured for NiPc-$^{\alpha}$OBu in toluene. This similarity suggests that they again represent relaxation from S_1 to the ($3d_{z^2}^1$, $3d_{x^2-y^2}^1$) state and thermalization on the ($3d_{z^2}^1$, $3d_{x^2-y^2}^1$) state. This assignment leaves two possibilities for ligation: (1) ligation occurs rapidly following formation of the ($3d_{z^2}^1$, $3d_{x^2-y^2}^1$) state or (2) ligation occurs more slowly but is unobserved by OTA measurements in the visible region. In the former scenario, the time constant for ligation must be similar to or faster than the 3 ps time constant for relaxation from S_1 to the ($3d_{z^2}^1$, $3d_{x^2-y^2}^1$) state, preventing a large population of the four-coordinate unligated ($3d_{z^2}^1$, $3d_{x^2-y^2}^1$) state from accumulating. In this scenario, ligation is effectively unobserved

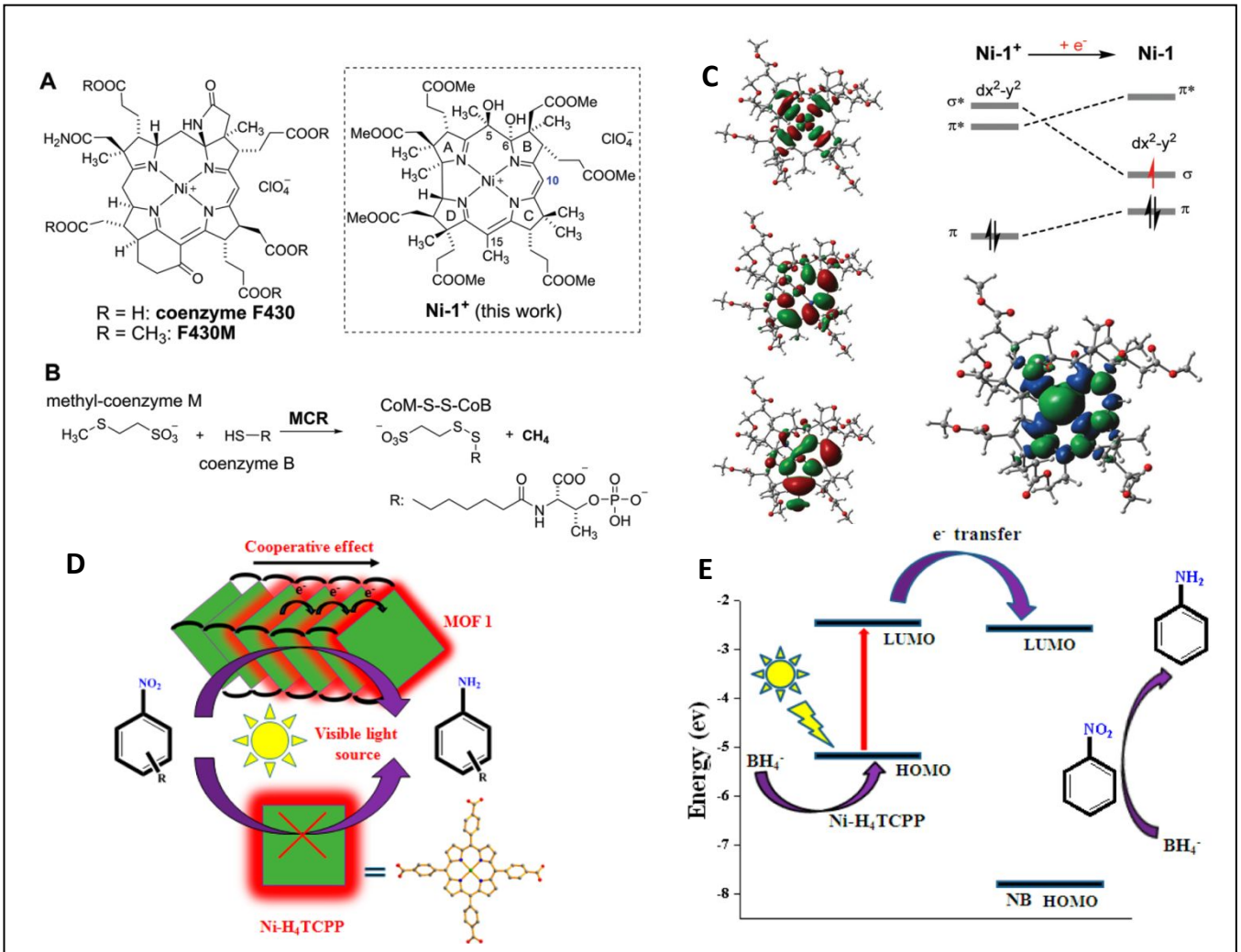

Figure. 9. Ni-corphin to mimic coenzyme F430; A) molecular structure, B) catalytic reactions, C) calculated molecular orbitals showing the energy lowering of the $3d_{x^2-y^2}$ orbital, relevant to the catalytic activities. Nickel porphyrin MOF materials; D) reaction scheme showing the necessity of having porphyrin arrays in order to perform catalytic reaction; E) energy levels of the reaction. A, B, C reproduced from Ref. 109 with permission from the Royal Society of Chemistry. D, E reprinted with permission from *Inorg. Chem.*, 2016, **55**, 5320. Copyright 2016 American Chemical Society.

and the 16 ps time constant corresponds to thermalization of the six-coordinate ligated ($3d_{z2}^1$, $3d_{x2-y2}^1$) state. Furthermore, the first-derivative-like lineshape, showing a shift of the Q band to higher energy, indicates that the phthalocyanine skeleton is more planar in the six-coordinate ligated ($3d_{z2}^1$, $3d_{x2-y2}^1$) state than in the four-coordinate unligated ($3d_{z2}^1$, $3d_{x2-y2}^1$) state.

In the latter scenario, ligation happens more slowly, but does not lead to a substantial perturbation of the phthalocyanine Q band. In this scenario, the differences in the OTA lineshapes observed for NiPc-$^{\alpha}$OBu in toluene and pyridine result entirely from solvation effects, excluding ligation. While the OTA spectra are not sensitive enough to the Ni electronic configuration, an excited-state ligation time constant faster than 20 ps is consistent with the process completing by 100 ps, as was observed in the XTA measurement for NiPc-$^{\alpha}$OBu in pyridine. The 100 ps XTA spectra clearly supports rapid formation of the six-coordinate ligated ($3d_{z2}^1$, $3d_{x2-y2}^1$) state, regardless of the exact mechanism. The excited-state dynamics of NiPc-$^{\alpha}$OBu in both non-coordinating and coordinating solvents are summarized schematically in Figure 8. Future XTA studies performed at XFEL facilities could distinguish the precise ligation mechanism in NiPc complexes by observing the Ni pre-edge and $1s \rightarrow 4p_z$ features with sub-picosecond time resolution. The dramatic increase in excited-state ligation rates for NiPc complexes compared to NiP complexes could have significant implications for the molecular design of Ni(II) photocatalysts. Furthermore, the analysis of the photoexcited NiP and NiPc complexes discussed here emphasizes how OTA, which is most sensitive to ligand-centered states, and XTA, which is most sensitive to metal-centered states, can be used cooperatively to deduce detailed electronic and structural excited-state trajectories.

7. Impact of Excited-State Structural Dynamics Studies on Photocatalysis using Nickel Complexes

The above sections described how XTA spectroscopy captured the excited-state trajectory, showing the transient oxidation state and coordination state evolution of the nickel centers. The immediate application of such approaches will be in capturing photocatalytic reaction intermediates and thus the reaction mechanisms, which could guide chemical syntheses to optimize the intended functions. Here, we compile three types of Ni-centered catalysts and photocatalysts emerging in the recent literature to provide perspective on the potential applications of XTA spectroscopy to enhance our understanding of their catalytic reaction mechanisms.

As we learned from the NiTMP and NiPc studies, the macrocycle size and planarity could affect the 3d orbital energy levels and the stability of potentially catalytic Ni(I) species. Coenzyme F430 (Figure 9) consists of a Ni-ion in a corphin ligand and is required by the enzyme methyl-coenzyme-M-reductase (MCR) for the last step of bacterial formation of CH_4 from CO_2.[108] To mimic the catalytic function in the enzyme, Ni(II)-tetrahydrocorphinate, Ni(II)-tetramethylcyclam or Ni(II)-didehydrocorrin complexes were embedded in a protein.[109] These molecules have only three of the four meso-carbon (C_{α}) atoms and, thus, smaller cavities that apparently stabilized the Ni(I) species to mimic the F430 function. Electrochemical studies with the model compound have demonstrated one-electron reduction of the inactive Ni(II) to a catalytically active Ni(I) state. XTA spectroscopy could then aid to (1) capture the possible Ni(I) species with the XANES signatures revealed by the NiTMP excited state and (2) resolve the ligation state of the nickel center to see if CO_2 binds to the metal center during the electro- or photochemical catalytic processes.

Other NiPc and NiP developments include (1) electrocatalytic reduction of CO_2 to CO by NiPc,[110, 111] where X-ray absorption spectra have been used to understand the induction effects of ligand substituents and correlate the Ni electronic configuration with catalytic yields, (2) catalytic activity of NiP in the water oxidation reaction[112] and (3)

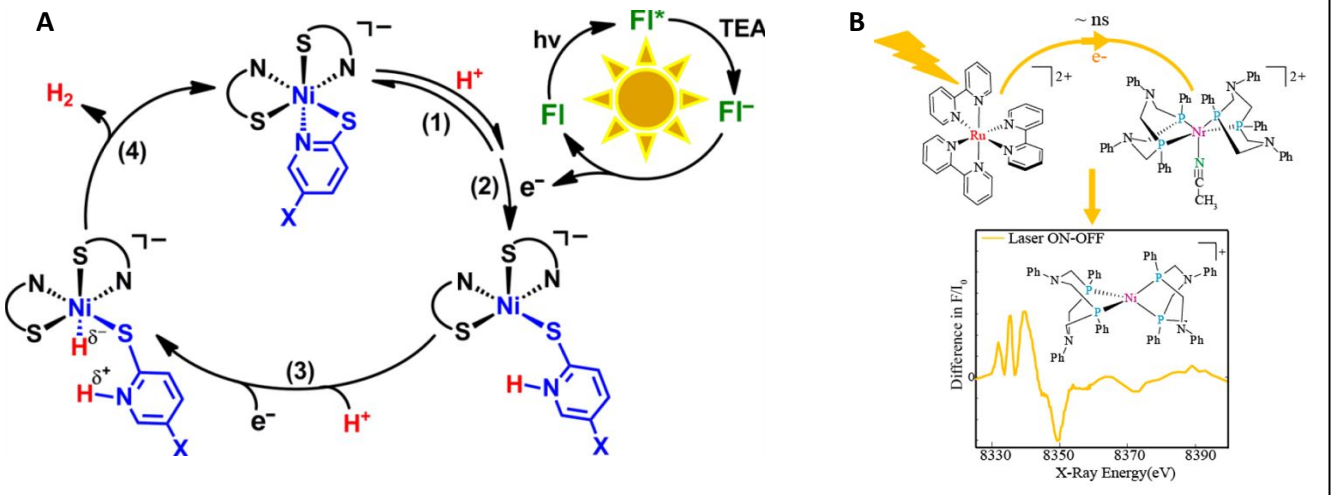

Figure 10. A). Nickel thiolate complex in bimolecular hydrogen generation reaction; B) bimolecular solar hydrogen generation with nickel catalyst studied by XTA. A reprinted from *J. Am. Chem. Soc.*, 2013, **135**, 14659. Copyright 2013 American Chemical Society. B reprinted from *J. Phys. Chem. C*, 2016, **120**, 20049. Copyright 2016 American Chemical Society.

construction of catalytically active metal—organic frameworks (MOF) using the Ni(II) porphyrin tetracarboxylic acid (Ni–H_4TCPP) building blocks.[113] The MOF showed photocatalytic activities for the reduction of various nitroaromatics, which formed the corresponding amines with high yield and selectivity. However, solutions of Ni–H_4TCPP did not exhibit photocatalytic activity under similar conditions. Such different catalytic behaviors suggest the cooperative electronic interactions between Ni-H_4TCPP and the Ni_3 oxo clusters in the MOF, which lead to the high catalytic performance of the MOF sample over solutions of Ni–H_4TCPP. To understand the details of these interactions, XTA at the Ni K-edge could be powerful for identifying the redox centers in the MOF. Having two types of nickel sites—one in the porphyrin macrocycle and three in the Ni_3 oxo cluster—could complicate the identification of the reaction intermediates, though, due to the overlap of the signals from both types of nickel species. However, if proper reference compounds and principle component analysis can be used, it is still possible to extract the transient oxidation state of the two nickel species in the Ni-H_4TCPP excited state and other catalytic intermediates following photoexcitation.

Nickel heterocyclic complexes play important roles in hydrogen generation from water splitting. Ideally, one could drive the reaction with sunlight, but solar hydrogen generation requires coupling the photoexcited states of individual molecules with multiple charge redox reactions. Thus, how to couple light sensitization, charge separation, charge accumulation, and ultimately solar fuel generation is one of the grand challenges in solar energy conversion. Therefore, several photocatalytic systems for water splitting used a bimolecular approach with separate molecules for light sensitizer and catalyst. Ni(II) thiolate complexes $(Et_4N)Ni(X\text{-}pyS)_3$[114, 115] with square planar and octahedral coordination geometry have been used as active catalysts for photocatalytic and electrocatalytic production of hydrogen, when coupled with fluorescein (Fl) as the photosensitizer (PS) and triethylamine (TEA) as the sacrificial electron donor.[115, 116]

A key to the activity of these catalysts is the reversible dechelation and protonation of the pyridine N atoms, which enable an internal heterocoupling of a metal hydride and an N-bound proton to produce H_2. Another example of the bimolecular light sensitizer and catalyst combination is an XTA study on the $[Ru(bpy)_3]^{2+}/[Ni(PPh_2NPh_2)_2(CH_3CN)]^{2+}$/ascorbic acid photocatalytic system probing the nano- to microsecond time regime, where the diffusion-controlled electron transfer between the excited $[Ru(bpy)_3]^{2+}$ and the nickel(II) proton reduction catalyst was detected on the nanosecond time scale, followed by formation of a transient distorted tetrahedral Ni(I) intermediate.[117] An increase in the lifetime of the Ni(I) species shows that the favored catalytic pathway occurs through reductive quenching of the excited PS followed by electron transfer to the catalyst. All these catalytic reactions can be

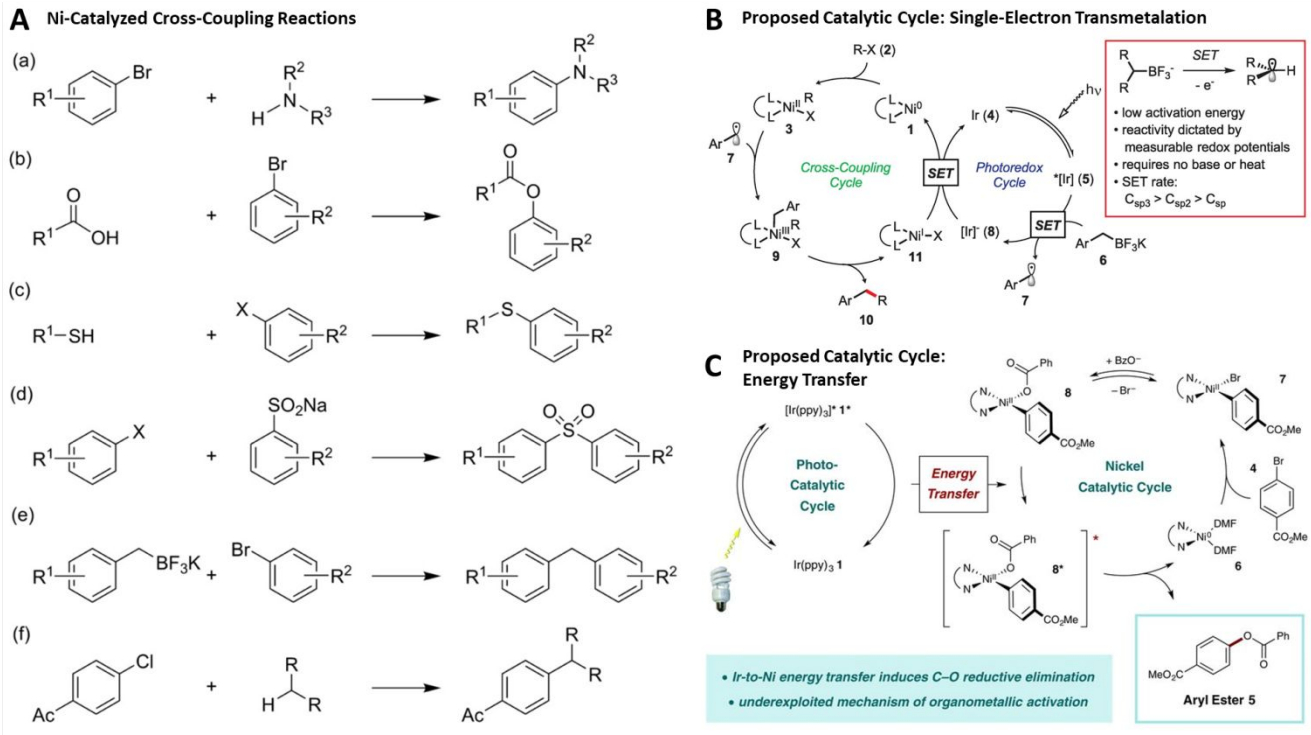

Figure 11. (A) Examples of Ni-catalyzed cross-coupling reactions demonstrated in the literature along with two proposed photodriven catalytic cycles involving (B) electron transfer and (C) energy transfer from the photosensitizer to the catalyst. A reprinted from *Chem. Eur. J.*, 2020, **27**, 2270 with permission (copyright 2020 Wiley-VCH GmbH). B from *Science*, 2014, **345**, 433. Reprinted with permission from AAAS. C from *Science*, 2017, **355**, 380. Reprinted with permission from AAAS.

investigated by XTA spectroscopy to gain insight into reaction mechanisms.

A third class of compounds, Ni-based cross-coupling catalysts, received significant attention recently for their ability to catalyze a wide variety of cross-coupling reactions, including many traditionally considered challenging.[118, 119] These catalysts typically comprise a Ni(II) center with square-planar geometry ligated by 2,2'-bipyridine and the two reagents in the cross-coupling reaction, though other variants exist as well. From the extensive investigations of the Ni-catalyzed cross-coupling reactions, several mechanisms emerged as the probable catalytic pathways (Figure 11).[119-122] The mechanisms propose numerous changes in oxidation state, coordination number, and ligation of the Ni catalyst intermediates, which X-ray absorption spectra measured in both the XANES and EXAFS regions are uniquely suited to identify. Furthermore, many of these reactions can be driven using photosensitizers, typically $Ir(bpy)_3^{2+}$, and even by direct excitation of the Ni catalyst.

Photosensitization of Ni-catalyzed cross-coupling reactions was proposed to occur via several mechanisms, including elementary reactions such as reduction of intermediates from Ni(I) to Ni(0) and oxidation of intermediates from Ni(II) to Ni(III)[120, 121] or generation of Ni(II) excited states via energy transfer from the photosensitizer.[122] The proposed photosensitization pathways and intermediates were based on thorough mechanistic studies using a variety of methods, including time-resolved optical and infrared spectroscopic techniques,[123-126] theoretical calculations of potential energy surfaces,[127] and detailed yield analyses.[122] These studies suggest different elementary photosensitization reactions are at play for different complexes or cross-coupling reactions and demonstrate the breadth of intermediates and reactions relevant to Ni-catalyzed cross-coupling reactions (Figure 11B,C). Steady-state and transient X-ray absorption spectroscopy can be used to obtain more direct measurements of the Ni centers throughout the cross-coupling reactions. Additionally, XTA measurements could be performed at the appropriate energy for transition-metal-center photosensitizers, such as $Ir(bpy)_3^{2+}$, enabling one to distinctly track the mechanistic steps of both the photosensitizer and catalyst.

As was demonstrated in the prior discussion of NiP and NiPc photophysics, X-ray absorption measurements can be used to precisely determine the coordination environment around the Ni center, the oxidation state of the Ni center, and the electronic configuration of the Ni center. For example, XTA measurements could clarify whether direct excitation of the Ni catalysts lead to excited states with (d,d) or MLCT character and whether these are general properties or specific to individual catalysts. Furthermore, the sensitivity of the X-ray absorption spectrum enables direct investigation of the effects that substituent groups on the bpy and aryl ligands have on the Ni center, which can also be correlated with observables such as reaction intermediates and yields. Insight from XTA measurements could be used to better understand the structure-function relationships and to fine-tune the performance in the myriad Ni-catalyzed reactions discussed in this section.

8. Summary and Outlook

We reviewed previous studies of the excited-state electronic and structural dynamics of NiP and NiPc complexes. We summarized how these two classes of transition metal complexes followed similar electronic relaxation pathways following optical excitation of the ligand $\pi \rightarrow \pi^*$ transition, beginning in the ligand-centered singlet (π, π^*) excited state, then rapidly relaxing to the metal-centered Ni ($3d_{z^2}^1$, $3d_{x^2-y^2}^1$) excited state, and finally returning to the ground state on the time scale of hundreds of picoseconds. Ultrafast XTA measurements on NiTMP even identified a short-lived charge-transfer Ni(I) (π, $3d_{x^2-y^2}^1$) intermediate state populated en route from the (π, π^*) to ($3d_{z^2}^1$, $3d_{x^2-y^2}^1$) excited state. Despite the similar electronic dynamics of NiP and NiPc, the XTA measurements reveal differences in the structural dynamics of the two types of complexes. NiPc was found to undergo rapid excited-state ligation in coordinating solvents on the timescale of tens of picoseconds, while excited-state ligation in NiP proceeds more slowly, on the timescale of hundreds of picoseconds. Additionally, we demonstrated that NiP exists in a broader distribution of structural conformers, some of which may facilitate the ground-state ligation that was observed for NiP, but not NiPc, complexes.

Lastly, we discussed numerous Ni-based photocatalysts, including catalysts for diverse applications such as solar fuels production and C–C cross-coupling reactions. These photocatalytic reactions undergo similar excited-state electronic and structural processes, such as oxidation or reduction, changes in the *d*-orbital electronic configuration, and ligation. The fundamental studies on NiP and NiPc complexes demonstrate the ability of XTA to clearly identify the different electronic and structural factors and lay the groundwork for use in better understanding the photocatalytic mechanisms of the systems previewed in Section 7. The information gained from XTA spectroscopy on these photocatalytic systems can help elucidate key catalyst properties, which then enable synthetic chemists to rationally tune and modify these materials for optimized performance.

Author Contributions

All of the authors wrote and edited manuscript. LXC provided an overall supervision and all authors participated in the original research activities resulted in the publications cited in the perspective.

Conflicts of interest

There are no conflicts to declare.

Acknowledgements

We acknowledge support for this work from the Solar Energy Photochemistry program (experimental work) and Ultrafast Initiative (theoretical work) of the U. S. Department of Energy, Office of Science, Office of Basic Energy Sciences, through Argonne National

Laboratory under Contract No. DE-AC02-06CH11357. Use of the Advanced Photon Source (APS) at ANL is supported by the U.S. Department of Energy, Office of Science, Office of Basic Energy Sciences under Contract No. DE-AC02-06CH11357. Linac Coherent Light Source (LCLS), SLAC National Accelerator Laboratory, is supported by the U.S. Department of Energy, Office of Sci-ence, Office of Basic Energy Sciences under Contract No. DE-AC02-76SF00515.

References

1. K. E. Dalle, J. Warnan, J. J. Leung, B. Reuillard, I. S. Karmel and E. Reisner, *Chemical Reviews*, 2019, **119**, 2752-2875.
2. L. Hammarstrom, *Accounts of Chemical Research*, 2015, **48**, 840-850.
3. K. J. Young, L. A. Martini, R. L. Milot, R. C. Snoeberger, V. S. Batista, C. A. Schmuttenmaer, R. H. Crabtree and G. W. Brudvig, *Coordination Chemistry Reviews*, 2012, **256**, 2503-2520.
4. K. Kalyanasundaram and M. Graetzel, *Current Opinion in Biotechnology*, 2010, **21**, 298-310.
5. H. Dau, C. Limberg, T. Reier, M. Risch, S. Roggan and P. Strasser, *Chemcatchem*, 2010, **2**, 724-761.
6. S. Romain, L. Vigara and A. Llobet, *Accounts of Chemical Research*, 2009, **42**, 1944-1953.
7. S. Ardo and G. J. Meyer, *Chemical Society Reviews*, 2009, **38**, 115-164.
8. S. Campagna, F. Puntoriero, F. Nastasi, G. Bergamini and V. Balzani, in *Photochemistry and Photophysics of Coordination Compounds I*, eds. V. Balzani and S. Campagna, 2007, vol. 280, pp. 117-214.
9. G. J. Meyer, *Inorganic Chemistry*, 2005, **44**, 6852-6864.
10. A. F. Heyduk and D. G. Nocera, *Science*, 2001, **293**, 1639-1641.
11. K. Kalyanasundaram and M. Gratzel, *Coordination Chemistry Reviews*, 1998, **177**, 347-414.
12. J. D. Knoll, B. A. Albani and C. Turro, *Accounts of Chemical Research*, 2015, **48**, 2280-2287.
13. G. Aubock and M. Chergui, *Nature Chemistry*, 2015, **7**, 629-633.
14. A. El Nahhas, C. Consani, A. M. Blanco-Rodriguez, K. M. Lancaster, O. Braem, A. Cannizzo, M. Towrie, I. P. Clark, S. Zalis, M. Chergui and A. Vlcek, *Inorganic Chemistry*, 2011, **50**, 2932-2943.
15. G. J. Hedley, A. Ruseckas and I. D. W. Samuel, *Chemical Physics Letters*, 2008, **450**, 292-296.
16. G. B. Shaw, C. D. Grant, H. Shirota, E. W. Castner, G. J. Meyer and L. X. Chen, *Journal of the American Chemical Society*, 2007, **129**, 2147-2160.
17. A. Gabrielsson, F. Hartl, H. Zhang, J. R. L. Smith, M. Towrie, A. Vlcek and R. N. Perutz, *Journal of the American Chemical Society*, 2006, **128**, 4253-4266.
18. D. J. Liard, M. Busby, P. Matousek, M. Towrie and A. Vlcek, *Journal of Physical Chemistry A*, 2004, **108**, 2363-2369.
19. D. Kuciauskas, J. E. Monat, R. Villahermosa, H. B. Gray, N. S. Lewis and J. K. McCusker, *Journal of Physical Chemistry B*, 2002, **106**, 9347-9358.
20. N. H. Damrauer and J. K. McCusker, *Journal of Physical Chemistry A*, 1999, **103**, 8440-8446.
21. J. P. Collin, A. Harriman, V. Heitz, F. Odobel and J. P. Sauvage, *Journal of the American Chemical Society*, 1994, **116**, 5679-5690.
22. M. Pizl, A. Picchiotti, M. Rebarz, N. Lenngren, Y. L. Liu, S. Zalis, M. Kloz and A. Vlcek, *Journal of Physical Chemistry A*, 2020, **124**, 1253-1265.
23. S. Yoon, P. Kukura, C. M. Stuart and R. A. Mathies, *Molecular Physics*, 2006, **104**, 1275-1282.
24. F. V. A. Camargo, T. Nagahara, S. Feldmann, J. M. Richter, R. H. Friend, G. Cerullo and F. Deschler, *Journal of the American Chemical Society*, 2020, **142**, 777-782.
25. F. D. Fuller and J. P. Ogilvie, in *Annual Review of Physical Chemistry, Vol 66*, eds. M. A. Johnson and T. J. Martinez, 2015, vol. 66, pp. 667-690.
26. G. S. Schlau-Cohen, A. Ishizaki and G. R. Fleming, *Chemical Physics*, 2011, **386**, 1-22.
27. M. Delor, I. V. Sazanovich, M. Towrie, S. J. Spall, T. Keane, A. J. Blake, C. Wilson, A. Meijer and J. A. Weinstein, *Journal of Physical Chemistry B*, 2014, **118**, 11781-11791.
28. C. R. Baiz, P. L. McRobbie, J. M. Anna, E. Geva and K. J. Kubarych, *Accounts of Chemical Research*, 2009, **42**, 1395-1404.
29. N. H. C. Lewis and G. R. Fleming, *Journal of Physical Chemistry Letters*, 2016, **7**, 831-837.
30. T. A. A. Oliver and G. R. Fleming, *Journal of Physical Chemistry B*, 2015, **119**, 11428-11441.
31. H. T. Lemke, C. Bressler, L. X. Chen, D. M. Fritz, K. J. Gaffney, A. Galler, W. Gawelda, K. Haldrup, R. W. Hartsock, H. Ihee, J. Kim, K. H. Kim, J. H. Lee, M. M. Nielsen, A. B. Stickrath, W. K. Zhang, D. L. Zhu and M. Cammarata, *Journal of Physical Chemistry A*, 2013, **117**, 735-740.
32. C. Bressler and M. Chergui, in *Annual Review of Physical Chemistry, Vol 61*, eds. S. R. Leone, P. S. Cremer, J. T. Groves, M. A. Johnson and G. Richmond, 2010, vol. 61, pp. 263-282.
33. C. Bressler, C. Milne, V. T. Pham, A. ElNahhas, R. M. van der Veen, W. Gawelda, S. Johnson, P. Beaud, D. Grolimund, M. Kaiser, C. N. Borca, G. Ingold, R. Abela and M. Chergui, *Science*, 2009, **323**, 489-492.
34. L. X. Chen, in *Annual Review of Physical Chemistry*, 2005, vol. 56, pp. 221-254.
35. L. X. Chen, *Angewandte Chemie-International Edition*, 2004, **43**, 2886-2905.
36. C. Bressler and M. Chergui, *Chemical Reviews*, 2004, **104**, 1781-1812.
37. M. Saes, C. Bressler, R. Abela, D. Grolimund, S. L. Johnson, P. A. Heimann and M. Chergui, *Physical Review Letters*, 2003, **90**.
38. L. X. Chen, G. B. Shaw, I. Novozhilova, T. Liu, G. Jennings, K. Attenkofer, G. J. Meyer and P. Coppens, *Journal of the American Chemical Society*, 2003, **125**, 7022-7034.
39. L. X. Chen, G. Jennings, T. Liu, D. J. Gosztola, J. P. Hessler, D. V. Scaltrito and G. J. Meyer, *Journal of the American Chemical Society*, 2002, **124**, 10861-10867.
40. L. X. Chen, W. J. H. Jager, G. Jennings, D. J. Gosztola, A. Munkholm and J. P. Hessler, *Science*, 2001, **292**, 262-264.
41. *X-Ray Absorption and X-Ray Emission Spectroscopy: Theory and Applications*, John Wiley & Sons, 2016.
42. L. X. Chen, X. Zhang and M. L. Shelby, *Chemical Science*, 2014, **5**, 4136-4152.
43. H. Michel and J. Deisenhofer, *The photosynthetic reaction center from the purple bacterium Rhodopseudomonas viridis: aspects of membrane protein structure*, 1990.
44. C. K. Chan, T. J. DiMagno, L. X. Q. Chen, J. R. Norris and G. R. Fleming, *Proc. Natl. Acad. Sci. U. S. A.*, 1991, **88**, 11202-11206.
45. M. R. Wasielewski, *Chemical Reviews* 1992, **92**, 435-461.
46. J.-P. Collin, A. Harriman, V. Heitz, F. Odobel and J.-P. Sauvage, *Coordination Chemistry Reviews*, 1996, **148**, 63-69.
47. J. S. Lindsey, *NATO ASI Series, Series C: Mathematical and Physical Sciences*, 1997, **499**, 517-528.
48. J. A. Shelnutt, K. Alston, E. W. Findsen, M. R. Ondrias and J. M. Rifkind, *ACS Symp. Ser.*, 1986, **321**, 232-247.
49. C. F. Martens, N. N. Murthy, H. V. Obias and K. D. Karlin, *Journal*, 1996, 629-630.
50. S. Franzen, L. Kiger, C. Poyart and J.-L. Martin, *Biophysical Journal*, 2001, **80**, 2372-2385.
51. J. P. Collman, C. J. Sunderland, K. E. Berg, M. A. Vance and E. I. Solomon, *Journal of the American Chemical Society*, 2003, **125**, 6648-6649.
52. A. J. Morris, G. J. Meyer and E. Fujita, *Accounts of Chemical Research*, 2009, **42**, 1983-1994.
53. J. H. Alstrum-Acevedo, M. K. Brennaman and T. J. Meyer, *Inorganic Chemistry*, 2005, **44**, 6802-6827.
54. H. L. Anderson, *Chemical Communications*, 1999, DOI: 10.1039/a904209a, 2323-2330.
55. F. D'Souza and O. Ito, *Coordination Chemistry Reviews*, 2005, **249**, 1410-1422.
56. D. Holten, D. F. Bocian and J. S. Lindsey, *Accounts of Chemical Research*, 2002, **35**, 57-69.
57. Q. Wang, W. M. Carnpbell, E. E. Bonfantani, K. W. Jolley, D. L. Officer, P. J. Walsh, K. Gordon, R. Humphry-Baker, M. K. Nazeeruddin and M. Gratzel, *Journal of Physical Chemistry B*, 2005, **109**, 15397-15409.
58. C. J. Chang, M. C. Y. Chang, N. H. Damrauer and D. G. Nocera, *Biochimica Et Biophysica Acta-Bioenergetics*, 2004, **1655**, 13-28.
59. G. Deinum, J. R. Stone, G. T. Babcock and M. A. Marletta, *Biochemistry*, 1996, **35**, 1540-1547.
60. D. A. Offord, S. B. Sachs, M. S. Ennis, T. A. Eberspacher, J. H. Griffin, C. E. D. Chidsey and J. P. Collman, *Journal of the American Chemical Society*, 1998, **120**, 4478-4487.
61. S. C. Tang, S. Koch, G. C. Papaefthymiou, S. Foner, R. B. Frankel, J. A. Ibers and R. H. Holm, *Journal of the American Chemical Society*, 1976, **98**, 2414-2434.
62. T. A. Betley, Q. Wu, T. Van Voorhis and D. G. Nocera, *Inorganic Chemistry*, 2008, **47**, 1849-1861.
63. D. K. Dogutan, R. McGuire and D. G. Nocera, *Journal of the American Chemical Society*, 2011, **133**, 9178-9180.
64. S. G. Kruglik, P. Mojzes, Y. Mizutani, T. Kitagawa and P. Y. Turpin, *Journal of Physical Chemistry B*, 2001, **105**, 5018-5031.
65. Y. Mizutani and T. Kitagawa, *Bulletin of the Chemical Society of Japan*, 2002, **75**, 965-971.
66. Y. Mizutani, Y. Uesugi and T. Kitagawa, *Journal of Chemical Physics*, 1999, **111**, 8950-8962.
67. J. L. Retsek, C. M. Drain, C. Kirmaier, D. J. Nurco, C. J. Medforth, K. M. Smith, I. V. Sazanovich, V. S. Chirvony, J. Fajer and D. Holten, *Journal of the American Chemical Society*, 2003, **125**, 9787-9800.

68. E. S. Ryland, K. L. Zhang and J. Vura-Weis, *Journal of Physical Chemistry A*, 2019, **123**, 5214-5222.
69. M. L. Shelby, P. J. Lestrange, N. E. Jackson, K. Haldrup, M. W. Mara, A. B. Stickrath, D. L. Zhu, H. T. Lemke, M. Chollet, B. M. Hoffman, X. S. Li and L. X. Chen, *Journal of the American Chemical Society*, 2016, **138**, 8752-8764.
70. M. L. Shelby, M. W. Mara and L. X. Chen, *Coordination Chemistry Reviews*, 2014, **277**, 291-299.
71. X. Y. Zhang, E. C. Wasinger, A. Z. Muresan, K. Attenkofer, G. Jennings, J. S. Lindsey and L. X. Chen, *Journal of Physical Chemistry A*, 2007, **111**, 11736-11742.
72. L. X. Chen, X. Zhang, E. C. Wasinger, J. V. Lockard, A. B. Stickrath, M. W. Mara, K. Attenkofer, G. Jennings, G. Smolentsev and A. Soldatov, *Chemical Science*, 2010, **1**.
73. D. Kim, C. Kirmaier and D. Holten, *Chem. Phys.*, 1983, **75**, 305-322.
74. D. Kim and D. Holten, *Chem. Phys. Lett.*, 1983, **98**, 584-589.
75. L. X. Chen, X. Zhang, E. C. Wasinger, K. Attenkofer, G. Jennings, A. Z. Muresan and J. S. Lindsey, *J. Am. Chem. Soc.*, 2007, **129**, 9616-9618.
76. L.-S. Kau, D. J. Spira-Solomon, J. E. Penner-Hahn, K. O. Hodgson and E. I. Solomon, *J. Am. Chem. Soc.*, 1987, **109**, 6433-6442.
77. A. Britz, B. Abraham, E. Biasin, T. B. van Driel, A. Gallo, A. T. Garcia-Esparza, J. Glownia, A. Loukianov, S. Nelson, M. Reinhard, D. Sokaras and R. Alonso-Mori, *Physical Chemistry Chemical Physics*, 2020, **22**, 2660-2666.
78. R. Chatterjee, C. Weninger, A. Loukianov, S. Gul, F. D. Fuller, M. H. Cheah, T. Fransson, C. C. Pham, S. Nelson, S. Song, A. Britz, J. Messinger, U. Bergmann, R. Alonso-Mori, V. K. Yachandra, J. Kern and J. Yano, *Journal of Synchrotron Radiation*, 2019, **26**, 1716-1724.
79. B. Pattengale, Q. H. Liu, W. H. Hu, S. Z. Yang, P. L. He, S. L. Tender, Y. Q. Wang, X. Y. Zhang, Z. C. Zhou, J. Zhang and J. E. Huang, *Journal of Physical Chemistry C*, 2019, **123**, 17994-18000.
80. R. Schweitzer-Stenner, C. Lemke, R. Haddad, Y. Qiu, J. A. Shelnutt, J. M. E. Quirke and W. Dreybrodt, *Journal of Physical Chemistry A*, 2001, **105**, 6680-6694.
81. J. A. Shelnutt, S. A. Majumder, L. D. Sparks, J. D. Hobbs, C. J. Medforth, M. O. Senge, K. M. Smith, M. Miura, L. Luo and J. M. E. Quirke, *Journal*, 1992, **23**, 523-529.
82. D. Kim and T. Sprio, *J. Am. Chem. Soc.*, 1986, **108**, 2099-2100.
83. H. S. Eom, S. C. Jeoung, D. Kim, J.-H. Ha and Y.-R. Kim, *J. Phys. Chem. A*, 1997, **101**, 3661-3669.
84. J. L. Retsek, C. M. Drain, C. Kirmaier, D. J. Nurco, C. J. Medforth, K. M. Smith, I. V. Sazanovich, V. S. Chirvony, J. Fajer and D. Holten, *j. Am. Chem. Soc.*, 2003, **125**, 9787–9800.
85. J. Rodriguez and D. Holten, *J. Chem. Phys.*, 1990, **92**, 5944-5950.
86. L. X. Chen, W. J. H. Jäger, G. Jennings, D. J. Gosztola, A. Munkholm and J. P. Hessler, *Science*, 2001, **292**, 262-264.
87. L. Campbell and S. Mukamel, *Journal of Chemical Physics*, 2004, **121**, 12323-12333.
88. L. Campbell, S. Tanaka and S. Mukamel, *Chemical Physics*, 2004, **299**, 225-231.
89. M. W. Renner, L. R. Furenlid, K. M. Barkigia, A. Forman, H. K. Shim, D. J. Simpson, K. M. Smith and J. Fajer, *J. Am. Chem. Soc.*, 1991, **113**, 6891-6898.
90. K. M. Barkigia, M. W. Renner, M. O. Senge and J. Fajer, *J. Phys. Chem. B*, 2004, **108**, 2173-2180.
91. M. Gouterman, *Journal of Molecular Spectroscopy*, 1961, **6**, 138-163.
92. A. M. Schaffer and M. Gouterman, *Theoretica chimica acta*, 1972, **25**, 62-82.
93. A. M. Schaffer, M. Gouterman and E. R. Davidson, *Theoretica chimica acta*, 1973, **30**, 9-30.
94. T. C. Gunaratne, A. V. Gusev, X. Peng, A. Rosa, G. Ricciardi, E. J. Baerends, C. Rizzoli, M. E. Kenney and M. A. J. Rodgers, *The Journal of Physical Chemistry A*, 2005, **109**, 2078-2089.
95. G. Balakrishnan, A. V. Soldatova, P. J. Reid and T. G. Spiro, *Journal of the American Chemical Society*, 2014, **136**, 8746-8754.
96. T. Fukuda, S. Homma and N. Kobayashi, *Chemistry – A European Journal*, 2005, **11**, 5205-5216.
97. E. A. Kuzmina, T. V. Dubinina, N. E. Borisova and L. G. Tomilova, *Macroheterocycles*, 2017, **10**, 520-525.
98. A. G. Martynov, J. Mack, A. K. May, T. Nyokong, Y. G. Gorbunova and A. Y. Tsivadze, *ACS Omega*, 2019, **4**, 7265-7284.
99. A. V. Soldatova, J. Kim, X. Peng, A. Rosa, G. Ricciardi, M. E. Kenney and M. A. J. Rodgers, *Inorganic Chemistry*, 2007, **46**, 2080-2093.
100. D. Rais, P. Toman, J. Černý, M. Menšík and J. Pfleger, *The Journal of Physical Chemistry A*, 2014, **118**, 5419-5426.
101. J. Hong, M. S. Kelley, M. L. Shelby, D. K. Hayes, R. G. Hadt, D. Rimmerman, X. Zhang and L. X. Chen, *ChemSusChem*, 2018, **11**, 2421-2428.
102. S. A. Krasnikov, A. B. Preobrajenski, N. N. Sergeeva, M. M. Brzhezinskaya, M. A. Nesterov, A. A. Cafolla, M. O. Senge and A. S. Vinogradov, *Chemical Physics*, 2007, **332**, 318-324.
103. R. R. Millard and B. I. Greene, *The Journal of Physical Chemistry*, 1985, **89**, 2976-2978.
104. J. Hong, T. J. Fauvell, W. Helweh, X. Zhang and L. X. Chen, *Journal of Photochemistry and Photobiology A: Chemistry*, 2019, **372**, 270-278.
105. R. Englman and J. Jortner, *Molecular Physics*, 1970, **18**, 145-164.
106. Y. Song, R. E. Haddad, S.-L. Jia, S. Hok, M. M. Olmstead, D. J. Nurco, N. E. Schore, J. Zhang, J.-G. Ma, K. M. Smith, S. Gazeau, J. Pécaut, J.-C. Marchon, C. J. Medforth and J. A. Shelnutt, *Journal of the American Chemical Society*, 2005, **127**, 1179-1192.
107. Y. Uesugi, Y. Mizutani and T. Kitagawa, *The Journal of Physical Chemistry A*, 1998, **102**, 5809-5815.
108. U. Ermler, W. Grabarse, S. Shima, M. Goubeaud and R. K. Thauer, *Science*, 1997, **278**, 1457-1462.
109. C. Brenig, L. Mosberger, O. Blacque, R. Kissner and F. Zelder, *Chemical Communications*, 2021, **57**, 7260-7263.
110. X. Zhang, Y. Wang, M. Gu, M. Wang, Z. Zhang, W. Pan, Z. Jiang, H. Zheng, M. Lucero, H. Wang, G. E. Sterbinsky, Q. Ma, Y.-G. Wang, Z. Feng, J. Li, H. Dai and Y. Liang, *Nature Energy*, 2020, **5**, 684-692.
111. X. Wang, Y. Fu, D. Tranca, K. Jiang, J. Zhu, J. Zhang, S. Han, C. Ke, C. Lu and X. Zhuang, *ACS Applied Energy Materials*, 2021, **4**, 2891-2898.
112. C. Y. Liu, D. van den Bos, B. den Hartog, D. van der Meij, A. Ramakrishnan and S. Bonnet, *Angewandte Chemie-International Edition*, 2021, **60**, 13463-13469.
113. M. S. Deenadayalan, N. Sharma, P. K. Verma and C. M. Nagaraja, *Inorganic Chemistry*, 2016, **55**, 5320-5327.
114. Z. J. Han, L. X. Shen, W. W. Brennessel, P. L. Holland and R. Eisenberg, *Journal of the American Chemical Society*, 2013, **135**, 14659-14669.
115. Z. J. Han, W. R. McNamara, M. S. Eum, P. L. Holland and R. Eisenberg, *Angewandte Chemie-International Edition*, 2012, **51**, 1667-1670.
116. S. Inoue, Y. N. Yan, K. Yamanishi, Y. Kataoka and T. Kawamoto, *Chemical Communications*, 2020, **56**, 2829-2832.
117. D. Moonshiram, A. Guda, L. Kohler, A. Picon, S. Guda, C. S. Lehmann, X. Y. Zhang, S. H. Southworth and K. L. Mulfort, *Journal of Physical Chemistry C*, 2016, **120**, 20049-20057.
118. S. Z. Tasker, E. A. Standley and T. F. Jamison, *Nature*, 2014, **509**, 299-309.
119. O. S. Wenger, *Chemistry – A European Journal*, 2021, **27**, 2270-2278.
120. J. C. Tellis, D. N. Primer and G. A. Molander, *Science*, 2014, **345**, 433.
121. Z. Zuo, D. T. Ahneman, L. Chu, J. A. Terrett, A. G. Doyle and D. W. C. MacMillan, *Science*, 2014, **345**, 437.
122. E. R. Welin, C. Le, D. M. Arias-Rotondo, J. K. McCusker and D. W. C. MacMillan, *Science*, 2017, **355**, 380.
123. L. Tian, N. A. Till, B. Kudisch, D. W. C. MacMillan and G. D. Scholes, *Journal of the American Chemical Society*, 2020, **142**, 4555-4559.
124. S. I. Ting, S. Garakyaraghi, C. M. Taliaferro, B. J. Shields, G. D. Scholes, F. N. Castellano and A. G. Doyle, *Journal of the American Chemical Society*, 2020, **142**, 5800-5810.
125. L. Yang, H.-H. Lu, C.-H. Lai, G. Li, W. Zhang, R. Cao, F. Liu, C. Wang, J. Xiao and D. Xue, *Angewandte Chemie International Edition*, 2020, **59**, 12714-12719.
126. B. J. Shields, B. Kudisch, G. D. Scholes and A. G. Doyle, *Journal of the American Chemical Society*, 2018, **140**, 3035-3039.
127. D. A. Cagan, G. D. Stroscio, A. Q. Cusumano and R. G. Hadt, *The Journal of Physical Chemistry A*, 2020, **124**, 9915-9922.